Investigation of Ultrasonic Transducer Responses when Coupled with Solid Materials

by

© **Katelyn Joyce**

A thesis submitted to the School of Graduate Studies in partial fulfillment of the requirements for the degree of Master of Science (Physics).

Department of Physics and Physical Oceanography

Memorial University

September 2023

St. John's, Newfoundland and Labrador, Canada

Abstract

This research focuses on ultrasonic transducer responses and elastic wave propagation in solid materials. This work was inspired by previous studies in geophysics, and its applications span several disciplines, such as material science, medicine and civil engineering. Previous geophysical work used a non-destructive testing method to investigate whether the frequency of a single-cycle ultrasonic pulse is related to the magnitude of its non-linear interactions. This work was inconclusive because the elastic wave frequency before and after propagating through the material was inconsistent. Hence, this research focuses on the fundamentals of how to analyze single-cycle pulses after they've travelled through solids using the Fast Fourier Transform and attempts to identify the source of the reported frequency discrepancy. This unexpected frequency discrepancy leads us to two hypotheses: (1) the examined material possesses the capacity for frequency conversion, or (2) flaws in the experimental setup led to misleading results. To investigate these hypotheses, we conducted a series of experiments to establish the capabilities and limitations of our instruments. Before examining frequency conversion, it was essential to establish our setup's ability to generate and measure desired frequencies in the range of 50 kHz to 1 MHz. Using ultrasonic transducers to trigger wave propagation in various solid materials, we develop optimal operating parameters when coupling transducers to solid samples. The significance of this research lies in the understanding of how ultrasonic transducers couple with different materials. Although the motivation for this research lies in non-linear elasticity, these understandings apply to a diverse variety of fields. This contribution to the field of physics and instrumentation will lead to improved protocols for non-linear elastic data collection, ultimately enhancing our ability to measure and understand elastic wave propagation.

Acknowledgements

First and foremost, I would like to acknowledge my supervisors, Dr. Alison Malcolm & Dr. Kristin Poduska, for making this project possible. I sincerely thank you for your guidance and support. I also owe a huge thank you to all the students in their research group. It has been my pleasure to build friendships and learn from each of you.

I would like to thank my professors, Dr. Todd Andrews, Dr. Edward Kendall, Dr. Anand Yethiraj and Dr. Ronald Haynes. I would also like to thank all the faculty and staff in the Physics department. Especially Dr. Ivan Saika-Voivod, Dr. Len Zedel, Donna Coombs, John Jerrett, Fred Perry, and Edward Hayden, for their support and kindness.

I would like to thank the Natural Sciences and Engineering Research Council (NSERC) and Memorial University's School of Graduate Studies for their financial support.

I sincerely thank my teammates and coaches from the Memorial University varsity soccer team. It was my honour to captain this team and play alongside some of my best friends while representing our university and the province of Newfoundland and Labrador.

I thank my best friend, Brooklyn Kostiuk, for being like a sister to me and supporting me along the way.

Finally, I extend my utmost gratitude to my parents and my brother for their unconditional love and encouragement. Everything I do, I do for them.

Table of contents

Title page **i**

Abstract **ii**

Acknowledgements **iii**

Table of contents **iv**

List of tables **vii**

List of figures **viii**

List of abbreviations **xiv**

1 Introduction **1**

1.1 Wave Propagation 1

1.2 Ultrasonic Transducers 4

1.3 Nonlinear Elasticity 5

1.4 Motivation 7

1.5 Objectives 10

1.6 Thesis Outline 11

2 Equipment Testing and Uncoupled Conditions **13**

2.1 No Transducers . . . 13
2.1.1 Introduction . . . 13
2.1.2 Methods . . . 14
Experimental Setup . . . 14
Data Analysis: Fast Fourier Transform . . . 15
2.1.3 Results . . . 24
2.2 Uncoupled Transducers . . . 33
2.2.1 Introduction . . . 33
2.2.2 Methods . . . 33
Ultrasonic Transducers . . . 35
2.2.3 Results . . . 37

3 Coupled Transducers 43

3.1 Introduction . . . 43
3.2 Methods . . . 45
3.3 Results . . . 46
3.3.1 No Sample . . . 46
3.3.2 Linear Sample: Homogeneous Cement . . . 51
3.3.3 Nonlinear Samples . . . 59
Inhomogeneous Cement . . . 59
Sandstone . . . 63

4 Conclusions 68

4.1 Summary . . . 68
4.2 Future Work . . . 70

Bibliography 75

A Central Frequencies **80**

List of tables

3.1 Dimensions of sample materials. 46

A.1 Central frequencies. All FFT spectra were calculated using the entire raw data set, unless stated otherwise (*). The central frequency of all FFT spectra in this thesis are reported as the frequency where the maximum spectral intensity occurs. Each spectrum was fitted with a gaussian and the full width at half maximum (FWHM) was calculated and half this value is reported as the uncertainty (±) in the central frequency. 84

List of figures

1.1 A schematic depicting the direction of motion of particles in a solid in relation to the direction of wave propagation for (A) P-waves and (B) S-waves. 3

1.2 Linear and nonlinear stress-strain relationships. Adapted from [2]. . . . 6

1.3 A schematic of the transient wave dynamic acousto-elastic testing (TW-DAET) experimental setup. Connections and waveforms related to the pump and probe are shown in red and green, respectively. 8

1.4 Frequency of S-wave probe after propagating through TW-DAET setup with a sample of cement with an embedded network of evenly spaced (5mm) copper wires. All spectra have the same central frequency (300±100 kHz), regardless of the input frequency. Data collected by [17]. 9

2.1 Schematic of the experimental setup for our experiments where pulses are sent directly from the waveform generator to the oscilloscope, with no transducers. 15

2.2 Inverse relationship between frequency sampling (df) and time sampling (T), where T is the length of the recorded window. 18

2.3 Parameters affecting FFT Resolution. Data was obtained using the waveform generator to oscilloscope configuration. (A) The number of cycles is changed, and the frequency (100 kHz), time window (1x10^{-4} s) and number of points are fixed (7679). (B) The frequency is changed, and the number of cycles (4), time window (1x10^{-4} s) and number of points are fixed (7679). (C) The time window is changed, and the number of cycles (4), frequency (100 kHz) and number of points are fixed (7679). (D) The number of points is changed, and the number of cycles (4), time window (1x10^{-4} s) and frequency (100 kHz) are fixed. FFT peak widths increase with pulse frequency and decrease with the number of cycles in a pulse. 20

2.4 (A) Curve fitting a 1 MHz single-cycle pulse (orange) with a sine function of the same period (blue). (B) FFT of a 1 MHz single-cycle pulse (orange) and that of the function obtained from curve fitting (blue). This plot demonstrates that the period of our single-cycle pulse is indicative of a sharp and accurate peak in the frequency domain. Its FFT is broad and skewed towards lower frequencies due to the limitations associated with the FFT algorithm, not due to problems with our ability to control pulse frequency. 21

2.5 Demonstration of FFT peaks broadening with frequency when the number of cycles (3), the number of points per cycle (10), frequency resolution (df=16.7 kHz) and the total time (6x10^{-5} s) are fixed. This occurs due to the convolution of our signals with sinc functions of various widths, leading to increases in peak width at high frequencies when signals are padded due to a time interval corresponding to a non-integer number of periods. 25

2.6 Demonstration of FFT peaks broadening with frequency when the number of cycles (3) and the number of points per cycle (10) are fixed, and the time windows were chosen to reflect an integer number of periods (3). Each pulse has a different time window and, consequently, a different frequency resolution (df). This removes the effect of the sinc function by removing the padding, but leads to peaks broadening with frequency due to increases in df. 26

2.7 Single-cycle pulses transmitted directly from the generator to the oscilloscope. Each pulse has a different period. A small time window (0 to 2.5x10^{-6} s) of the raw data is shown to illustrate the differences in periods. 27

2.8 FFT spectra of single-cycle pulses transmitted directly from the generator to the oscilloscope. Each spectrum has a different central frequency (80±50 kHz, 300±200 kHz, 400±300 kHz, 600±500 kHz, 800±500 kHz). FFT spectra were calculated using the full raw data sets. 29

2.9 FFT spectra of 4-cycle pulses transmitted directly from the generator to the oscilloscope. Each spectrum has a different central frequency (100±20 kHz, 200±30 kHz, 400±50 kHz, 600±100 kHz, 800±100 kHz, and 1000±200 kHz) that is in agreement with the input frequency (legend). FFT spectra were calculated using the full raw data sets. 30

2.10 FFT spectra of continuous-cycle pulses transmitted directly from the generator to the oscilloscope. Each spectrum has a different central frequency (100±4 kHz, 200±4 kHz, 400±10 kHz, 600±10 kHz, 800±20 kHz, and 1000±20 kHz) that is in agreement with the input frequency (legend). FFT spectra were calculated using the full raw data sets. 31

2.11 Experimental setup for testing individual transducers using a laser vibrometer. 34

2.12 Olympus ultrasonic contact transducers. Our P-wave and S-wave transducers are identical in appearance but distinguishable by serial numbers. 36

2.13 Uncoupled S-transducers generating 1-cycle pulses. (A) Entire raw waveforms with a shaded region. (B) FFT spectra of the entire raw waveform shown in (A), df=10 kHz. Central frequencies are 40±20 kHz, 100±40 kHz, 120±50 kHz and 120±60 kHz. (C) FFT spectra of raw data were calculated using the data in the shaded region in (A), df=30 kHz. Central frequencies are 60±50 kHz, 120±40 kHz, 120±50 kHz, 120±60 kHz. 38

2.14 Time window selection affecting FFT spectrum and central frequency. (A) Raw data of a single-cycle 200 kHz pulse from S-transducers (blue) and a cropped region of the first cycle in the pulse (grey). (B) FFT of the full waveform from above (blue) and the cropped region (grey). Cropping the waveform causes the central frequency to shift from 120 kHz to 182 kHz, but it increases the frequency spacing (df) from 10 kHz to 182 kHz, significantly worsening the resolution. 41

2.15 FFT spectra of 10-cycle pulses generated by uncoupled (top) S-transducers and (bottom) P-transducers using the laser vibrometer setup. FFT spectra were calculated using the entire raw data sets. For all four transducers, the central frequencies of all pulses are in accordance with the input frequencies (S1: 50±2 kHz, 100±4 kHz and 200±10 kHz; S2: 50±3 kHz, 100±4 kHz and 200±10 kHz; P1: 50±3 kHz, 100±4 kHz and 200±10 kHz; P2: 50±3 kHz, 100±5 kHz and 200±10 kHz). 42

3.1 Expected signal resulting from S-transducers, highlighting the production of a parasitic P-wave. 44

3.2 Experimental setup of two-transducer pulse transmission technique. . . 46

3.3 Single-cycle pulses from P-wave transducers coupled together with no sample. (A) A small time window (0 to $3x10^{-6}$ s) of the raw data is shown to illustrate the differences in periods. (B) FFT spectra calculated from entire raw waveforms. Central frequencies are in accordance with input frequencies (see legend): 100±50 kHz, 180±100 kHz, 440±200 kHz, 600±300 kHz, 800±400 kHz, 800±400 kHz. 47

3.4 Single-cycle pulses from S-wave transducers coupled together with no sample. (A) A small time window ($-1x10^{-6}$ s to $3.5x10^{-6}$ s) of the raw data is shown to illustrate the differences in periods. (B) FFT spectra were calculated from entire raw waveforms. Central frequencies are in accordance with input frequencies (see legend): 200±50 kHz, 400±200 kHz, 700±300 kHz, 900±300 kHz and 900±300 kHz. 50

3.5 Single-cycle pulses from S-wave transducers coupled together with homogeneous cement. This figure illustrates (A) the time domain signals of the parasitic P-wave and (B) the FFT spectra of these signals. FFT spectra were calculated from entire raw waveforms. All spectra have the same central frequency of 400 kHz (see Appendix A for individual uncertainties) and are not in accordance with input frequency. 53

3.6 Single-cycle pulses from S-wave transducers coupled together with homogeneous cement. Figure (A) illustrates the time domain signals of the resulting S-wave and how the period of the S-wave part of a single-cycle pulse does not change with input frequency. Figure (B) illustrates the FFT spectra of these signals and how the central frequency of the S-wave part of a single-cycle pulse does not change with input frequency. FFT spectra were calculated from entire raw waveforms. All spectra have the same central frequency of 280 kHz (see Appendix A for individual uncertainties) and are not in accordance with input frequency. 55

3.7 Four-cycle pulses from S-wave transducers coupled together with homogeneous cement. This figure illustrates (A) the time domain signals of the parasitic P-wave and (B) the FFT spectra of these signals. FFT spectra were calculated from entire raw waveforms. The period of the first cycle of the parasitic P-wave is independent of the input parameters. 56

3.8 Four-cycle pulses from S-wave transducers coupled together with homogeneous cement. This figure illustrates (A) the time domain signals of the S-wave and (B) the FFT spectra of these signals. FFT spectra were calculated from entire raw waveforms. The period of the first cycle of the S-wave is independent of the input parameters 57

3.9 Single-cycle pulses from P-transducers coupled together with homogeneous cement. This figure illustrates (A) the time domain signals and (B) the FFT spectra of these signals. FFT spectra were calculated from entire raw waveforms. All spectra have different central frequencies (160±50 kHz, 280±90 kHz, 360±100 kHz, 500±200 kHz, 600±200 kHz, 700±300 kHz). 58

3.10 Inhomogeneous Cement coupled with S-wave transducers. This figure illustrates the S-wave part of a single-cycle signal. (a) Entire raw waveform in the time-domain. (b) FFT of raw time-domain data between 4.85x10^{-5} s and 6x10^{-5} s. All spectra have the same central frequency of 350±200 kHz and are not in accordance with input frequency. 61

3.11 Inhomogeneous cement coupled with S-wave transducers. This figure illustrates the parasitic P-wave part of a single-cycle signal. (a) Entire raw time-domain data and (b) the FFT spectra of these raw time-domain data. FFT spectra were calculated from entire raw waveforms. All spectra have the same central frequency of 600±200 kHz and are not all in accordance with input frequency. 62

3.12 Sandstone coupled with S-wave transducers. This figure illustrates the (A) entire time-domain data of the S-wave part of single-cycle pulses and the (b) FFT spectra of the entire time-domain signals. All spectra have the same central frequency of 300 kHz (see Appendix A for individual uncertainties) and are not in accordance with input frequency. 64

3.13 Sandstone coupled with S-wave transducers. This figure illustrates the entire time-domain data of the parasitic P-wave of a single-cycle pulse and (b) the FFT spectra of the entire signals. All signals possess the same central frequency of 160±200 kHz, and are not in agreement with input frequency. 66

4.1 FFT spectra of the parasitic P-wave component of single-cycle ultrasonic pulses after propagating through inhomogeneous cement (cement with an embedded network of evenly spaced (5mm) copper wires) coupled with S-wave transducers. (a) Figure 1.4 repeated. All signals possess the same central frequency of 300±100 kHz. (b) Figure 3.11 repeated. All signals possess the same central frequency of 600±200 kHz. 73

List of abbreviations

DAET	Dynamic Acousto-elastic Testing
FFT	Fast Fourier Transform
FWHM	Full Width at Half Maximum
P-wave	Pressure wave
S-wave	Shear wave
TW-DAET	Transient Wave Dynamic Acousto-elastic Testing

Chapter 1

Introduction

1.1 Wave Propagation

From ocean waves and sound waves to seismic waves and electromagnetic waves, waves are an integral part of our daily lives. Whether it's the ripple of the ground after an earthquake, the light that illuminates the sky, the sound of a roaring crowd, or a crowd doing *the* wave, waves are propagating all around us.

This study involves the propagation of ultrasonic waves through various solid materials. Hence, establishing an understanding of how waves propagate in solids is critical. The wave is a fundamental model of classical physics, and it describes a disturbance travelling through a medium. Mechanical perturbations provoke tiny disturbances in media, displacing particles from their positions of rest. The magnitude of these disturbances depends on the intrinsic elastic properties and mass density of the medium [12]. In solids, there are two distinct types of waves: compressional waves and shear waves [7], shown in Figure 1.1. Shear waves (S-waves) are transverse in nature, meaning the particles of the medium move perpendicular to the direction of

wave propagation. Some examples of transverse waves include ocean waves and seismic surface waves. In compressional waves or P-waves, also called longitudinal waves, the particles of the medium move in the direction of propagation. As P-waves propagate through a medium, the particles of said medium move parallel to the direction of propagation. This parallel motion results in regions of compression (high density) and rarefaction (low density). Sound waves are an example of longitudinal waves. This thesis employs both forms of mechanical waves in the context of non-destructive testing. For this reason, we focus on the propagation of elastic waves, where the stress-strain relationships in the solid obey Hooke's Law [7] (see section 1.3). Here, the particles in a solid oscillate about an equilibrium position and eventually return to their original state. In other words, elastic waves impose loads which are not severe enough to cause permanent damage [7].

Elastic waves can be characterized by parameters such as wavelength, frequency, amplitude, and speed. Wavelength, λ, is the distance between two neighbouring peaks or regions of compression. The wavelength encompasses a single cycle and is measured in meters. Frequency, f, describes how frequently oscillations are occurring, it is measured in Hertz (Hz) and is a measure of the number of cycles passing a fixed point per second. Frequency and wavelength are related by the following equation:

$$v = \lambda f \tag{1.1}$$

Here, v is the wave speed, measured in m/s. Wave speed describes the rate at which sound propagates through media and is characteristic of the medium [8]. Finally, amplitude is a parameter describing the magnitude or height of a wave. In this thesis, we employ the use of transducers, which convert pressure fluctuations to voltages. Hence, wave amplitude is measured in Volts. As a wave interacts with the

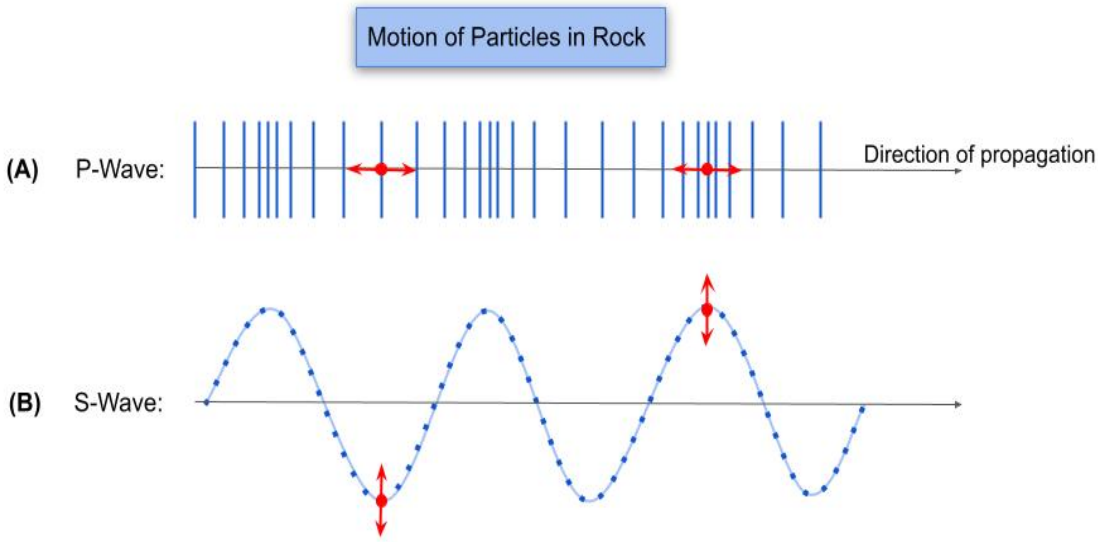

Figure 1.1: A schematic depicting the direction of motion of particles in a solid in relation to the direction of wave propagation for (A) P-waves and (B) S-waves.

particles in a medium, the wave amplitude decreases in a process called attenuation. The attenuation of mechanical energy in a solid may be attributed to various dissipative phenomena such as absorption, scattering, reflection, refraction, diffraction, interference, and divergence [14]. Among these classes, the primary contributors of attenuation in ultrasonic materials characterization are absorption and scattering [14], which are both frequency-dependant phenomena [6]. Absorption describes the process by which mechanical energy is lost during transmission through the medium, primarily due to heat transfer [7]. Scattering occurs when inhomogeneities in the medium, such as cracks and cavities, cause the direction of energy transmission to depart from its original path, resulting in less energy arriving at the detector [7]. Scattering is a complex process which depends on factors such as the average size of particles in relation to the wavelength and particle density [6]. A detailed and mathematical explanation of these processes can be found in Chapter 7 of [7] and [6, p. 127]. Central to this thesis, the frequency of a wave, in theory, depends only on the emission source and is independent of the material that it interacts with [8]. In reality, attenuation is frequency-dependant, meaning the frequency content of a wave changes with distance travelled through a medium [6]. Specifically, higher frequencies often attenuate faster with distance than lower frequencies [28].

1.2 Ultrasonic Transducers

Sound is a form of mechanical energy that propagates via longitudinal oscillations, leading to alternating regions of low-pressure (rarefaction) and high-pressure (compression). The human ear can detect sound waves within the frequency range of 20 Hz to 20,000 Hz [10]. Sound waves with frequencies below 20 Hz are classified as infrasound waves, whereas those greater than 20 kHz are labelled as ultrasound

[10]. A sound source, such as a tuning fork, produces longitudinal wave oscillations in the surrounding medium, causing energy to propagate through the medium. Just as strumming a guitar string or striking a tuning fork produces sound, ultrasonic waves can be produced using transducers.

Transducers are instruments that convert energy from one form to another [4]. Ultrasonic transducers are transducers that emit and detect ultrasound waves by converting between mechanical energy and electrical energy [8]. In ultrasonics, the sound source is often a piezoelectric material, such as lead zirconium titanate or quartz. Discovered in 1880 by the Curie brothers, piezoelectricity is a phenomenon which describes how applying an electric field in certain materials induces proportional dimensional changes, and vice-versa [4]. When a voltage is incident on a piezoelectric element within a transducer, the crystal vibrates and generates mechanical energy in the form of ultrasound waves. Conversely, when ultrasound waves arrive at the receiver, the mechanical energy is converted into a voltage, which can be measured using an oscilloscope.

1.3 Nonlinear Elasticity

Materials are made up of spring-like molecular bonds which expand and contract when subjected to various forces. Strain is a measure of the deformation of an object under stress, which is governed by the spring constant of these molecular bonds [11]. Specifically, elasticity is related to the strain, ϵ, induced in a material when an external stress, σ, is applied. Strain is a dimensionless quantity which describes an object's fractional change in length when it is subjected to stress. When an object with length L, is stretched or compressed by an amount ΔL, the strain is defined as $\Delta L/L$. Stress

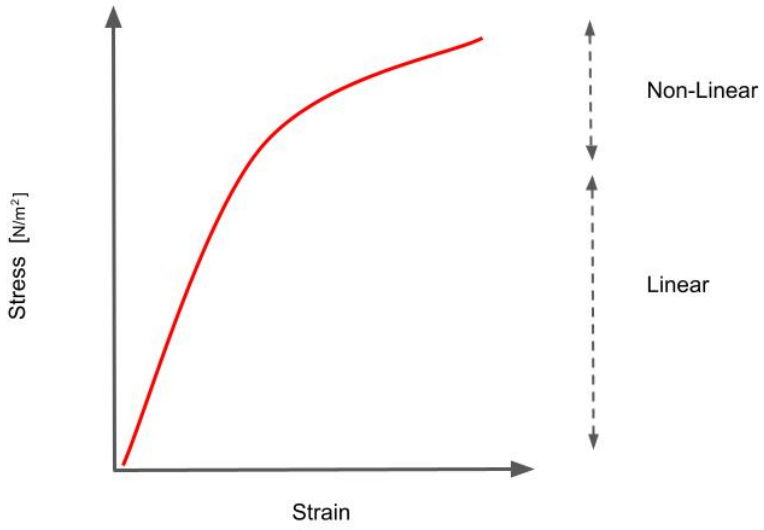

Figure 1.2: Linear and nonlinear stress-strain relationships. Adapted from [2].

is a measure of the force, F, applied over a cross-sectional area, A, and it is measured in N/m^2 [11]. Elasticity is often quantified in terms of Young's modulus, E, which describes how an object is stretched when pulled and compressed when loaded. When the induced strain is proportional to the applied stress, as shown in Figure 1.2, the material is deemed linearly elastic. Here, the stress–strain relationship adheres to Hooke's law, and Young's modulus is derived from the following equation [11]:

$$\sigma = E\epsilon \tag{1.2}$$

Soft materials with high elasticity, such as rubber, have a small Young's modulus, while rigid materials, such as steel, have a relatively large Young's modulus [11].

Nonlinear elasticity is defined as a deviation from Hooke's law [20], where the stress-strain relationship is nonlinear, as shown in Figure 1.2. The study of non-linear elasticity spans a wide variety of disciplines. Nonlinear elasticity is an indicator of

material damage (broken bonds, distorted bond angles, voids etc.) [21]. Therefore, it is used across fields such as geophysics, medicine, and civil engineering to characterize the structure of complex solids. For example, nonlinear elastic measurements are prominently applied to rocks [23], because it allows for an understanding of wave speed changes in the Earth's crust, which gives insight into earthquakes, fault slips, and tides [23]. In medicine, nonlinear ultrasound has been used to indicate accumulated damage in human bones, which can be indicative of osteoporosis [16]. Finally, the nonlinear elasticity of concrete has been investigated in the context of construction and characterizing building materials [30].

1.4 Motivation

The frequency dependence of nonlinear elasticity is an area of interest among researchers [22, 17]. Scientists are interested to see whether changing the frequency of elastic wave perturbations changes the nonlinear response induced in a material.

This thesis focuses on addressing a very specific problem we identified in the literature. That is, previous work conducted in our lab has created uncertainty as to our ability to dictate the frequency of elastic wave pulses [17]. This recent work employed a non-destructive testing method called Transient Wave Dynamic Acoustoelastic Testing (TW-DAET), shown in Figure 1.3. TW-DAET uses a pump and probe configuration to generate and sense ultrasonic elastic waves. It applies a transient perturbation load (pump) to the material while simultaneously interpreting wave speed changes in an elastic probe wave, which provides information on the nonlinear elastic behaviour of the sample. More information on the post-acquisition calculations used to relate travel time delays to non-linear elastic parameters can be found in [16, p.

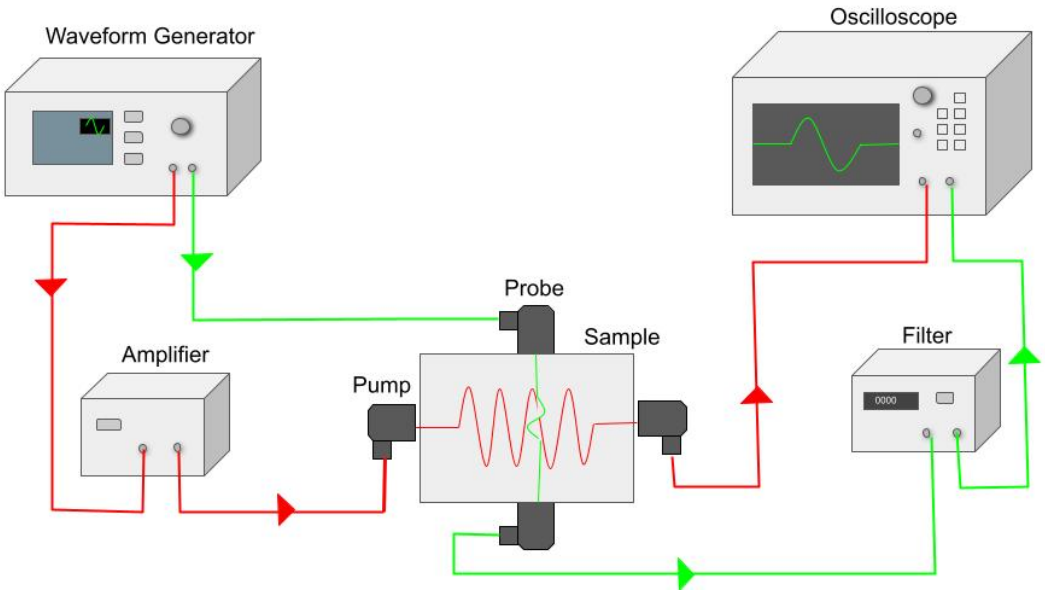

Figure 1.3: A schematic of the transient wave dynamic acousto-elastic testing (TW-DAET) experimental setup. Connections and waveforms related to the pump and probe are shown in red and green, respectively.

1499].

[17] reported that the nonlinear response increases when the wavelength of the elastic probe wave resembles the separation between known inhomogeneities in the samples. He suggests that this finding is evidence that there exists a probe wavelength dependency on the TW-DAET response. He concludes that his claim opens up the possibility that our ability to image inhomogeneities can be improved by tuning the frequency of the probe pulses. Upon closer inspection of the raw data [17] used to make the aforementioned claims, we discovered a discrepancy. The single most striking observation to emerge from the closer inspection of this data was that the frequency of the elastic waves did not change as the frequency parameter was changed on the generator (see Figure 1.4). The frequency of the single-cycle ultrasonic pulses was examined after propagating through the inhomogenous cement sample. When it

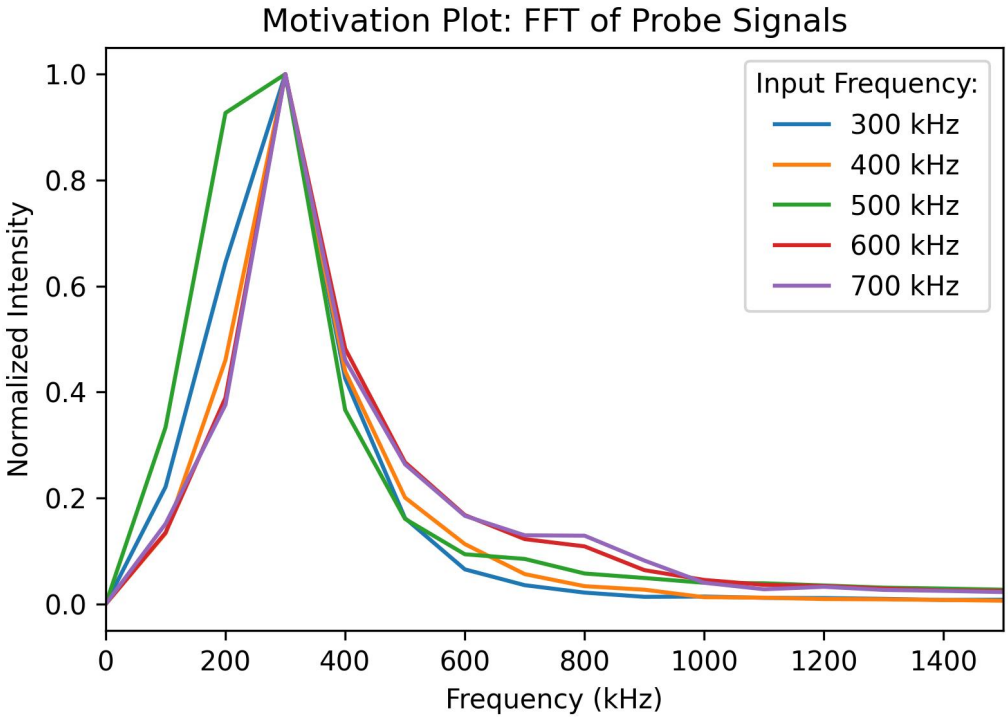

Figure 1.4: Frequency of S-wave probe after propagating through TW-DAET setup with a sample of cement with an embedded network of evenly spaced (5mm) copper wires. All spectra have the same central frequency (300±100 kHz), regardless of the input frequency. Data collected by [17].

was compared to the frequency which had been set on the waveform generator, it was found that the two were not in agreement. Pulses with input frequencies ranging from 300 kHz - 700 kHz were examined, and it was found that the frequency of the output pulses did not reflect their input parameters. Moreover, all spectra have the same central frequency (300±100 kHz), regardless of the input frequency, as illustrated in Figure 1.4. This experiment was conducted using a cement sample with an embedded network of evenly spaced (5 mm) copper wires and a 1 MHz S-wave probe transmitting single-cycle pulses and a 0.1 MHz S-wave pump (operating at 50 kHz) transmitting 4-cycle pulses.

1.5 Objectives

This study aims to identify the source of the discrepancy between input and output frequency in the TW-DAET configuration, as described in section 1.4. This unexpected result led us to several potential hypotheses. Firstly, and perhaps least likely, we consider the possibility that the examined material possesses the capacity for frequency conversion. That is, the inhomogeneities in the sample convert the frequency of elastic waves to some preferential frequency. Secondly, we consider the possibility that flaws in the experimental setup yield misleading results. Specifically, we hypothesize that our transducers behave differently when they are coupled to solid materials. There is not a lot published about how transducers behave when coupled with solids. We aim to address this gap in the literature and set up a protocol for testing this type of equipment.

To investigate these hypotheses, we conduct control experiments to establish the capabilities and limitations of our instruments. Before examining frequency conversion, it is essential to establish our setup's ability to generate and measure desired frequencies in the kilohertz range. Using ultrasonic transducers to trigger wave propagation in various solid materials, we develop best practices and optimal operating parameters when coupling media to new samples.

Improvements in non-destructive testing methods involving dynamic acousto-elastics would improve our ability to characterize non-linear elasticity. Specifically, this research will allow for the identification of potential problems in the existing TW-DAET setup and the optimization of the setup for future research. Should this study successfully identify the source of the frequency discrepancy, it would allow for further research into the relationship between elastic wave frequency and non-linear interactions. In geophysics, understanding the frequency dependence of nonlinear elasticity

is important because it facilitates comparisons between observations made at the laboratory scale and the field scale [22].

1.6 Thesis Outline

The experiments in this study are presented in three sections: (1) No Transducers, (2) Uncoupled Transducers, and (3) Coupled Transducers. To identify the source of the frequency discrepancy outlined in section 1.4, the experiments in this thesis are presented in a step-wise fashion of increasing complexity. Starting from the simplest case of a pulse sent directly from the waveform generator to the oscilloscope, and building towards the most complex case of the TW-DAET configuration. The objective of the first two sections was to evaluate the functionality of the equipment and establish a baseline for expected outputs. This involved conducting a series of control experiments to ensure that the equipment was operating properly and assessing the setup's ability to produce elastic waves with desired frequencies. The third component of this thesis involves evaluating the ability of S-wave and P-wave transducers to produce and sense elastic waves with desired frequencies under coupled conditions. That is, when they are fastened to a sample using a couplant and a bar clamp.

The remainder of this thesis document is organized into three chapters. Following this introductory chapter, Chapter 2 will outline the first two sets of experiments: No transducers and Uncoupled transducers. The first control experiment evaluates the waveform generator's ability to generate pulses with specific parameters and the oscilloscope's ability to sense said pulses, and the second control experiment assesses the responses of uncoupled transducers using a laser vibrometer. This chapter will also describe the data analysis approach used in this thesis and the limitations associated

with using the Fast Fourier Transform in this context. In Chapter 3, we present the results from the third and final set of experiments involving coupled transducers. Here, we analyze responses after propagating through a variety of coupled systems for both P-wave and S-wave transducers. Finally, Chapter 4 will act as the concluding chapter, where significant results will be summarized, and the broader implications of the study will be stated.

Chapter 2

Equipment Testing and Uncoupled Conditions

2.1 No Transducers

2.1.1 Introduction

This thesis addresses the viability of using a Transient Wave Dynamic Acousto-elastic Testing (TW-DAET) (see Figure 1.3) setup for investigating the relationship between the frequency of ultrasonic waves and their non-linear interactions. To do so, this study aims to identify the discrepancy between input and output frequency, as described in section 1.4. Firstly, in this chapter, we assess the functionality of the equipment used in the experimental setup. The first and simplest control experiment in this process is to assess the functionality of the waveform generator and the oscilloscope. This involves conducting tests to ensure that these devices are operating properly. Specifically, we assess their ability to produce and sense elastic waves with

various frequencies.

The perplexing results obtained by [17] suggested one of two things: either cement with an embedded copper network possesses frequency conversion properties. Or, flaws in the experimental setup lead to misleading results. This study will investigate the functionality of each component of the TW-DET configuration, first established in [5], to determine whether this apparent frequency conversion was a result of a flaw in the experimental setup or if this material possesses unique capabilities. In this chapter, we begin with the simplest case: no transducers or sample materials, just the function generator and the oscilloscope.

2.1.2 Methods

Experimental Setup

The first component of this study involves a series of control experiments to verify the functionality of our equipment. These experiments are presented in a step-wise fashion of increasing complexity, starting from the simplest case of a pulse sent directly from the waveform generator to the oscilloscope (shown in Figure 2.1), building towards a TW-DAET configuration.

Firstly, we connect the waveform generator (Keysight 33500B Series Waveform Generator) directly to the oscilloscope (Agilent Technologies InfiniiVision MSO-X 2014A Mixed Signal Oscilloscope) using coaxial cables. To eliminate any potential artifacts from our transducers and sample materials, this preliminary experiment aims to establish the generator's ability to properly generate the desired signal. This step allows us to examine whether the parameters we set on the function generator are truly impacting the properties of the elastic waves it produces. The two parameters

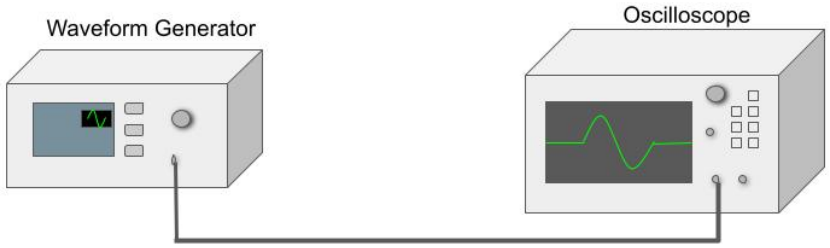

Figure 2.1: Schematic of the experimental setup for our experiments where pulses are sent directly from the waveform generator to the oscilloscope, with no transducers.

we adjust in this experiment are frequency and number of cycles. We begin with a series of single-cycle pulses over the range 100-1000 kHz. We repeat this process with a four-cycle pulse and a continuous pulse.

Data Analysis: Fast Fourier Transform

Using the Fast Fourier Transform (FFT) to determine the central frequency of a time-domain signal is a well-established technique [33, 24, 9, 27, 13]. Problems that are difficult to visualize in the time domain can be simplified by performing a transformation and analyzing signals in the frequency domain. The central frequency is the frequency at which the peak magnitude occurs in the frequency spectrum [27]. Throughout the entirety of this thesis, the uncertainty in the central frequency is given by fitting the region surrounding the central maximum of each spectrum with a Gaussian function and calculating the full width at half maximum (FWHM) of said

Gaussian. Half the value of the FWHM, rounded to one significant figure, is reported as the uncertainty in the central frequency.

The raw data from the control experiments are Comma Separated Values (CSV) files, consisting of two columns: time and voltage. Data in this form represents how the voltage arriving at the oscilloscope varies over time. As previously stated, the goal of Chapters 2 is to assess the functionality of our equipment and establish a baseline of expected output signals. Specifically, we aim to adjust the driving frequency set on the waveform generator and observe the corresponding change to the output signal on the oscilloscope. In order to analyze the frequency of the output signal, we use the Fast Fourier Transform (FFT). This mathematical transformation is a computational approximation to the well-established Fourier Transform. For a continuous function $f(t)$, the Fourier Transform, $F(\omega)$, is defined as follows: [3]

$$F(\omega) = \int_{-\infty}^{\infty} f(t) e^{-i\omega t} dt \tag{2.1}$$

Here, ω is the frequency content of the signal and t is time. In the case of discrete signals, the frequency domain can be accessed using the Discrete Fourier Transform (DFT), defined as follows: [3]

$$F(k\Delta f) = \sum_{n=0}^{N-1} f(n\Delta t) e^{-i(2\pi k \Delta f)(n\Delta t)} \tag{2.2}$$

Here, N is the number of data points collected in the time domain, and Δt is the spacing between these points, equal to T/N, where T is the total sampling time. The frequency increment, Δf, is equal to $1/T$, and it describes the spacing between points in the frequency domain. The DFT output, $F(k\Delta f)$, is a set of complex values indicating the relative contribution to the signal by each discrete frequency in the set

of multiples of the frequency increment, where $k = 0, 1, 2, ..N - 1$. In this thesis, we interpret the magnitude of each complex number in the set $F(k\Delta f)$.

The Fast Fourier Transform (FFT) is a computer algorithm which calculates the DFT in a time-efficient manner [3]. Using the programming language Python and NumPy's FFT routine [18], the FFT is applied to the raw data, bringing it from the time domain to the frequency domain. The result is a Fourier transform, where each bin on the independent axis corresponds to the contribution of the corresponding frequency in the signal. As a proof of concept, previous work generated single-cycle radio-frequency pulses and analyzed them using an oscilloscope and a spectrum analyzer [13], the latter using a FFT to analyze the pulse. Transforming our raw data into frequency space allows us to determine central frequencies and compare peak shifts quantitatively. The goal of our FFT analysis is not to measure absolute intensities but rather to compare FFT spectra at various input frequencies to see if we observe changes in the central frequency. Therefore, throughout this thesis, all frequency spectra are normalized. That is, all FFT magnitudes have been divided by their respective maximum to yield values ranging from 0 to 1, which we refer to as normalized intensity on the vertical axis.

As previously stated, frequency sampling, Δf, is the spacing between points in frequency space. For the remainder of this thesis, frequency sampling will be referred to as df. This resolution is controlled by the total time window of the raw data. The inverse relationship between time and frequency sampling is shown in Figure 2.2. The goal of TW-DAET is to detect fractional changes in travel times. Therefore, it is beneficial to collect data with the smallest feasible time-step. This ultimately equates to zooming in on the oscilloscope and recording a pulse with the smallest possible total time. The more finely we sample the time domain, the more accurately

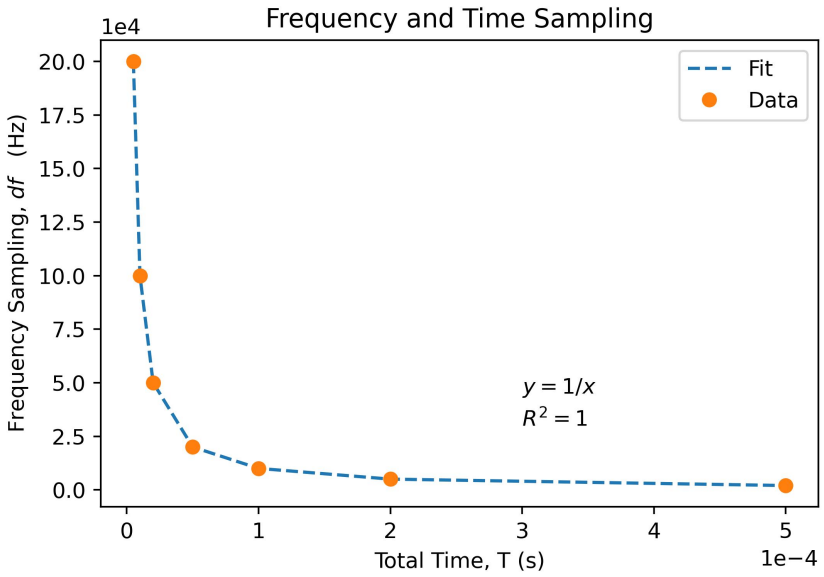

Figure 2.2: Inverse relationship between frequency sampling (df) and time sampling (T), where T is the length of the recorded window.

we can identify time delays. However, smaller *df* values do not necessarily equate to improved frequency resolution. This is because our ability to measure the frequency of an ultrasound pulse using the FFT algorithm is also governed by the width of the FFT peak and not solely *df*. As shown in Figure 2.2, the smaller the time window, the larger the value of *df*. This is a trade-off where reducing the total time examined in the time domain means reduced frequency resolution in the frequency domain. These data were collected using the generator to oscilloscope configuration (Figure 2.1) by varying the time window on the oscilloscope before saving the raw data. These data were fit with the function $y = 1/x$, yielding an R^2 value of 1.

Given that detecting frequency shifts is of particular interest in this thesis, we investigate which parameters control the width of the FFT peaks. Here, we consider peak width to be the frequency range covered by the base of a peak. Peak widths were compared by isolating four parameters: the frequency and number of cycles of

the input waveform (controlled on the waveform generator), the time window displayed on the oscilloscope and the number of data points collected (controlled on the oscilloscope). The results are presented in Figure 2.3. Figure 2.3 is a collection of data obtained using the waveform generator to oscilloscope configuration to study how the FFT spectrum is affected by the aforementioned parameters.

Our primary finding from Figure 2.3 is that peak width increases with frequency when other parameters are fixed. This means that the FFT resolution is inherently poorer for higher-frequency pulses. When the total time is fixed, peak width can be thought of as related to the ratio of how much of the total time is used for the pulse component of the signal. Padding the data with zeros does not narrow the peaks, as shown in Figure 2.3C. Rather, it causes interpolation using a sinc function. This improves the frequency sampling by reducing the value of df, but it does not improve frequency resolution (reduce the width of peaks). We find that adjusting the number of data points collected in the time domain (within the examined range) has no effect on the FFT (see Figure 2.3D). Although, we suspect that if the number of collected data points were small enough, aliasing would eventually occur. Finally, we observed that peak widths scale with frequency and are inversely proportional to the number of cycles. In Figure 2.3A, we demonstrate that peaks become narrower as we increase the number of periods. Therefore, in the case of a continuous wave, recording data over a longer period of time will yield narrower peaks because more cycles are recorded. Based on this observation, in our investigation, we focus on changing the frequency and the number of cycles of our pulses.

Using our knowledge of the relationship between FFT peak widths and the number of cycles per pulse, gained from Figure 2.3, we employ a curve-fitting exercise. The period of a wave is equal to the inverse of its frequency. Previous work leveraged this

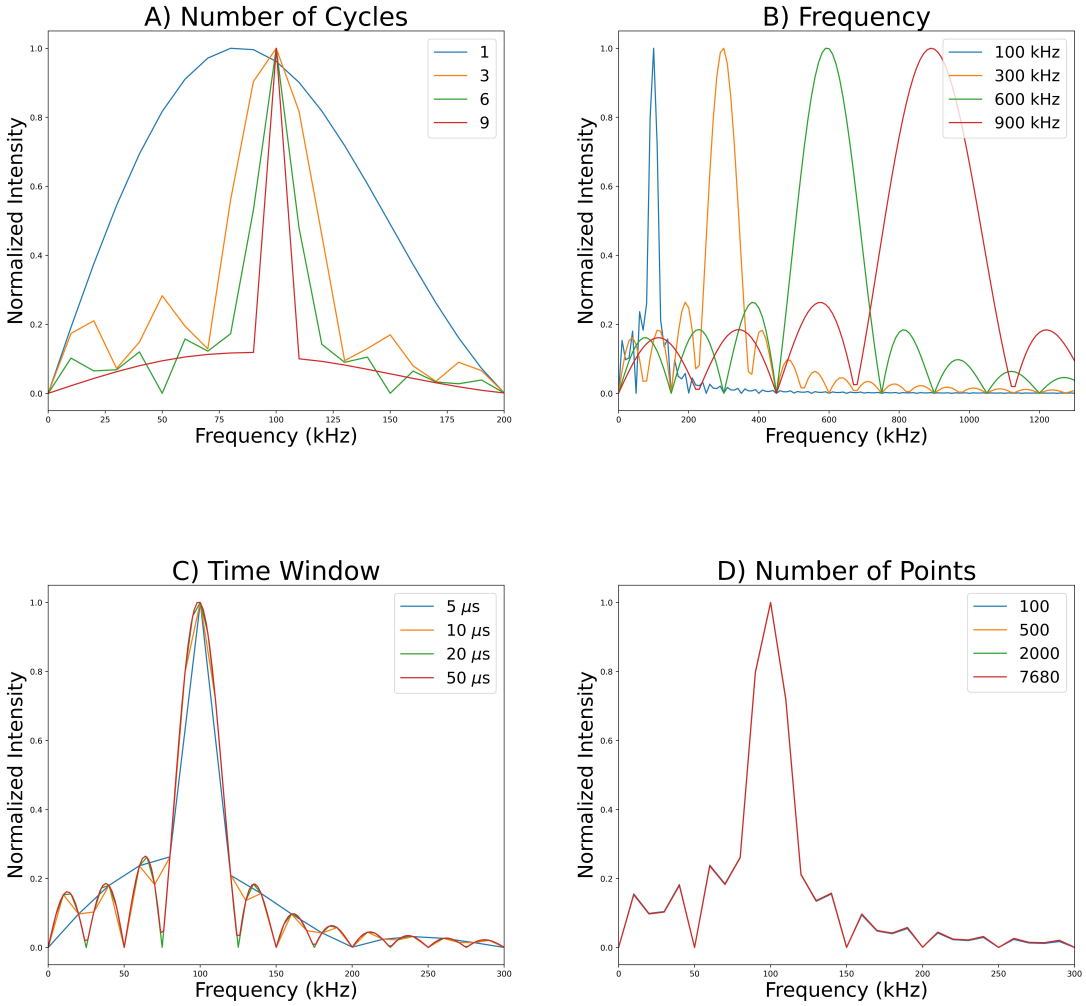

Figure 2.3: Parameters affecting FFT Resolution. Data was obtained using the waveform generator to oscilloscope configuration. (A) The number of cycles is changed, and the frequency (100 kHz), time window (1x10^{-4} s) and number of points are fixed (7679). (B) The frequency is changed, and the number of cycles (4), time window (1x10^{-4} s) and number of points are fixed (7679). (C) The time window is changed, and the number of cycles (4), frequency (100 kHz) and number of points are fixed (7679). (D) The number of points is changed, and the number of cycles (4), time window (1x10^{-4} s) and frequency (100 kHz) are fixed. FFT peak widths increase with pulse frequency and decrease with the number of cycles in a pulse.

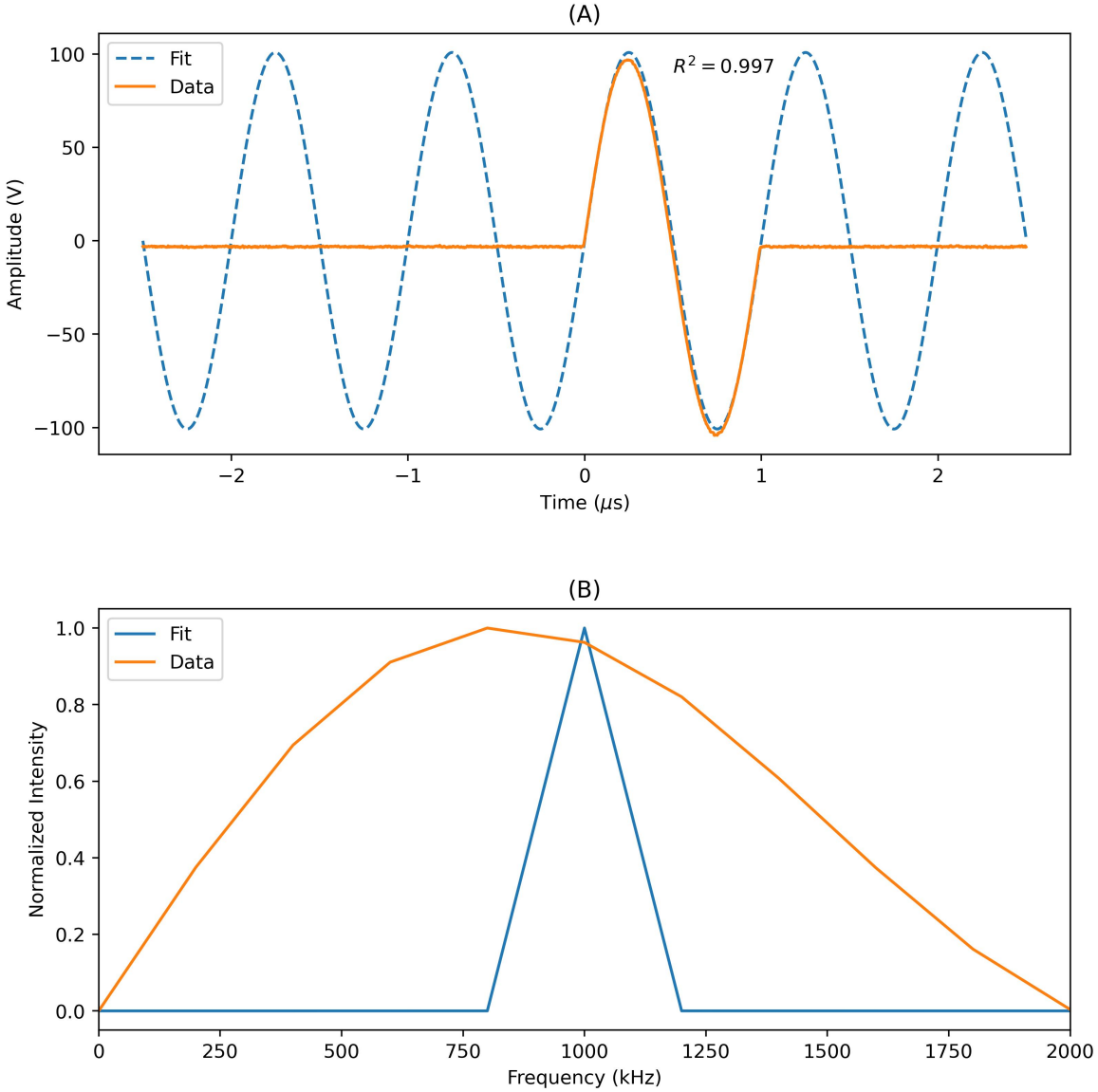

Figure 2.4: (A) Curve fitting a 1 MHz single-cycle pulse (orange) with a sine function of the same period (blue). (B) FFT of a 1 MHz single-cycle pulse (orange) and that of the function obtained from curve fitting (blue). This plot demonstrates that the period of our single-cycle pulse is indicative of a sharp and accurate peak in the frequency domain. Its FFT is broad and skewed towards lower frequencies due to the limitations associated with the FFT algorithm, not due to problems with our ability to control pulse frequency.

inverse relationship by measuring the period of single-cycle radio-frequency pulses and reporting the frequency corresponding to this period [13]. We employ this strategy by considering the period of our single-cycle pulse to be indicative of its central frequency. Hence, using the period as a method to quantitatively describe the frequency. The single-cycle pulse shown in Figure 2.4.A has an input frequency of 1 MHz. This pulse has a period of 1 microsecond, which corresponds to a frequency of 1 MHz. To further illustrate the limitation of using an FFT to measure the frequency of a single-cycle pulse, this single-cycle pulse was fitted with a sine function of the form $\mathrm{Asin}(2\pi ft)$ using the SciPy optimization and curve fitting package [29]. Using non-linear least squares, the curve fitting algorithm determines the optimal values for the parameters A and f to minimize the sum of the squared residuals. Here, the parameters A and f are the amplitude in Volts and the frequency in Hertz, respectively. The curve fitting process found that $A = 100.8$ V and $f = 1.009$ MHz are the parameters of best-fit, yielding an R^2 value of 0.997. This result reassures us that we are able to control the period (and consequently, the frequency) of the pulses leaving the waveform generator. In Figure 2.4.B we compare the FFT spectra from the single-cycle pulse and the curve of best-fit with the same period. The FFT of the single-cycle pulse (shown in orange) has a broad spectrum, spanning 2 MHz, and it reaches its maximum at 800 kHz. If we were to use peak frequency as a method of measuring absolute pulse frequency, this would lead us to conclude that the frequency of our pulse has shifted from 1 MHz to 800 kHz. However, when we consider the FFT of the fitted sine function with the same period as our pulse, we obtain a much narrower peak, which spans just 400 kHz and has a central frequency of 1 MHz. Both the data and the fitted curves have the same frequency sampling (df=200 kHz). However, the FFT of the fitted curve has a much narrower peak, indicating improved frequency resolution. Critically, this plot demonstrates that the period of our single-cycle pulse is indicative of a sharp peak

in the frequency domain, centred around 1 MHz. This tells us that the broad peak skewed towards lower frequencies is attributed to the limitations associated with using an FFT to measure the frequency of single-cycle pulses and is not indicative of issues with our ability to control pulse frequency. Given that both pulses have the same period, Figure 2.4 illustrates that central frequency is not a perfect indicator of the frequency of our pulse. To improve the quality of this quantitative measurement, we must increase the number of cycles in our pulse, or fit our pulse with a sine wave with the same period and analyze the frequency of the fitted sine wave.

Throughout this thesis, it is apparent that the central frequency of spectra becomes less reliable at higher frequencies. We have already demonstrated that this phenomenon is an artifact of our FFT routine and not indicative of our ability to transmit high-frequency pulses (see Figure 2.4). In an effort to explain the origin of this broadening, we use synthetic data to illustrate the parameters which govern the width of frequency spectra.

We begin by controlling parameters such as the number of cycles, the total time of data acquisition (and therefore, frequency sampling, df) and the number of data points per cycle sampled in the time domain. As shown in Figure 2.5, all synthetic data sets have different frequencies, denoted in the legend. The total time of acquisition was controlled by appending different amounts of zero-padding to each synthetic sinusoid, yielding a total time of 0.6 microseconds. From Figure 2.5 we see that peaks broaden with frequency, despite having the same number of points per cycle sampled in time and the same total time of data acquisition. Here, broadening is not a result of frequency spacing. Rather, the explanation for this broadening lies in the properties of the Fourier Transform pair: the sinc function and the boxcar function. Different frequencies require different amounts of time to complete a given number of cycles

and are therefore convolved with boxcar functions of various lengths. This equates to convolving our signals with sinc functions of various widths, leading to increases in peak width at high frequencies. We refer to this as the sinc phenomenon.

We take this demonstration one step further by carefully choosing time windows which allow for an integer number of periods. As shown in Figure 2.6, this practice generates sharp peaks with widths equal to $2df$.

From Figures 2.5 and 2.6, we see that peaks broadening with frequency is an inherent and unavoidable truth of the FFT. In the case of Figure 2.6, when we strategically select time windows leading to an integer number of periods we avoid convolving our signals with sinc functions of various widths. However, our resolution is then limited by df. Because higher frequencies have shorter periods, they require less time to complete a given number of cycles, resulting in larger df values and wider FFT peaks. On the other hand, if we control for df by choosing a fixed total time, higher frequencies require less time to complete a given number of cycles and are therefore convolved with a shorter boxcar function, resulting in broader spectra. We also observe that padding a signal with zeros does not change the shape of the frequency spectrum. Rather, it simply increases the total time of data acquisition, which in turn reduces df. As previously shown, a smaller df means finer sampling in the frequency domain, but does not equate to narrower peaks in our frequency spectra.

2.1.3 Results

We begin by presenting our raw data obtained from transmitting a series of single-cycle pulses over the range of 100-1000 kHz.

From Figure 2.7, we learn that the waveform generator can produce pulses with

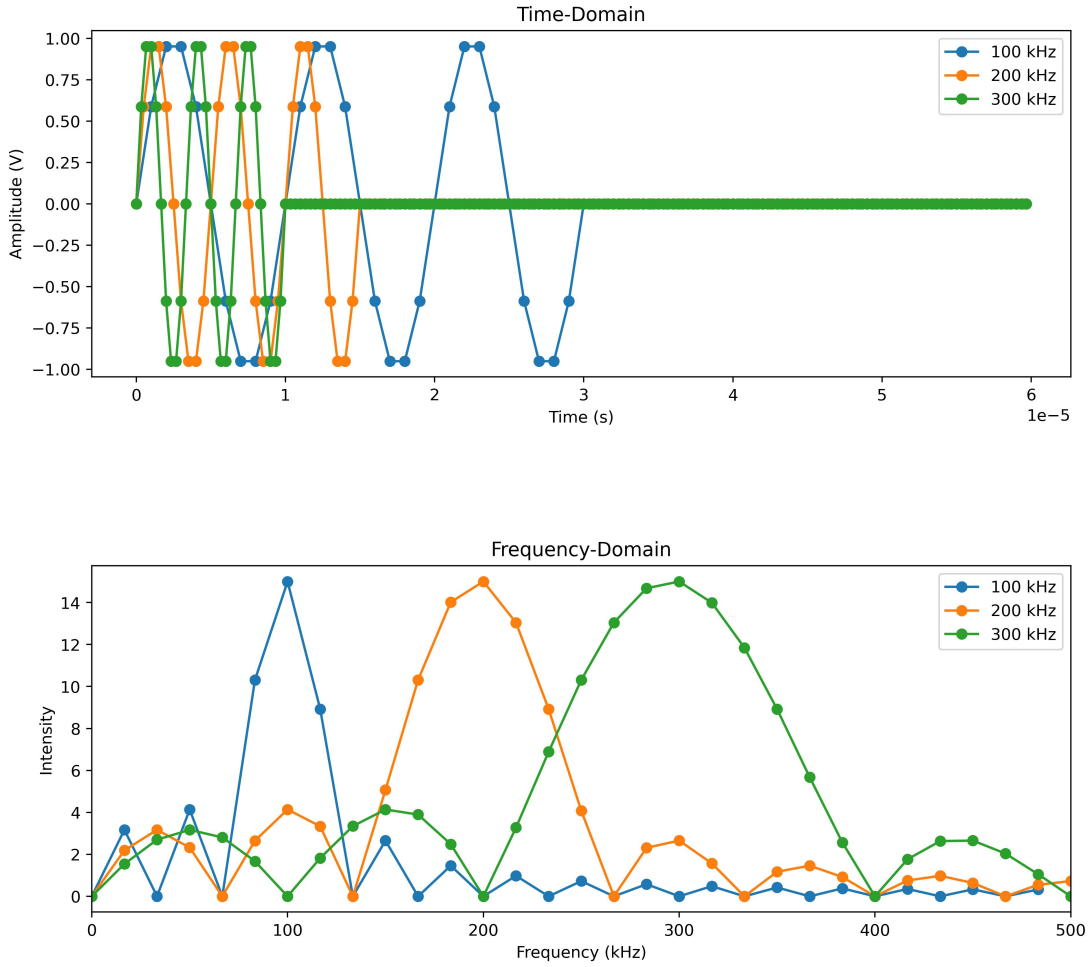

Figure 2.5: Demonstration of FFT peaks broadening with frequency when the number of cycles (3), the number of points per cycle (10), frequency resolution (df=16.7 kHz) and the total time (6x10^{-5} s) are fixed. This occurs due to the convolution of our signals with sinc functions of various widths, leading to increases in peak width at high frequencies when signals are padded due to a time interval corresponding to a non-integer number of periods.

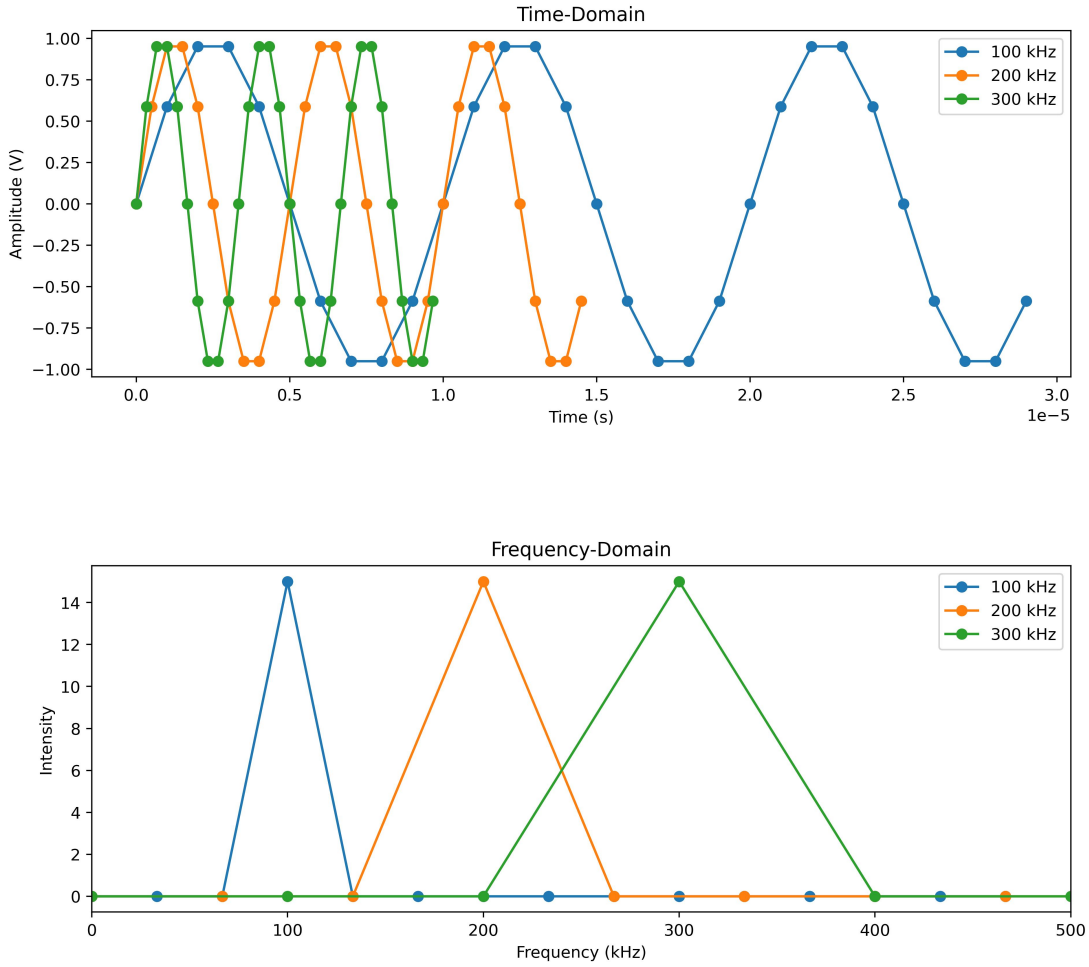

Figure 2.6: Demonstration of FFT peaks broadening with frequency when the number of cycles (3) and the number of points per cycle (10) are fixed, and the time windows were chosen to reflect an integer number of periods (3). Each pulse has a different time window and, consequently, a different frequency resolution (df). This removes the effect of the sinc function by removing the padding, but leads to peaks broadening with frequency due to increases in df.

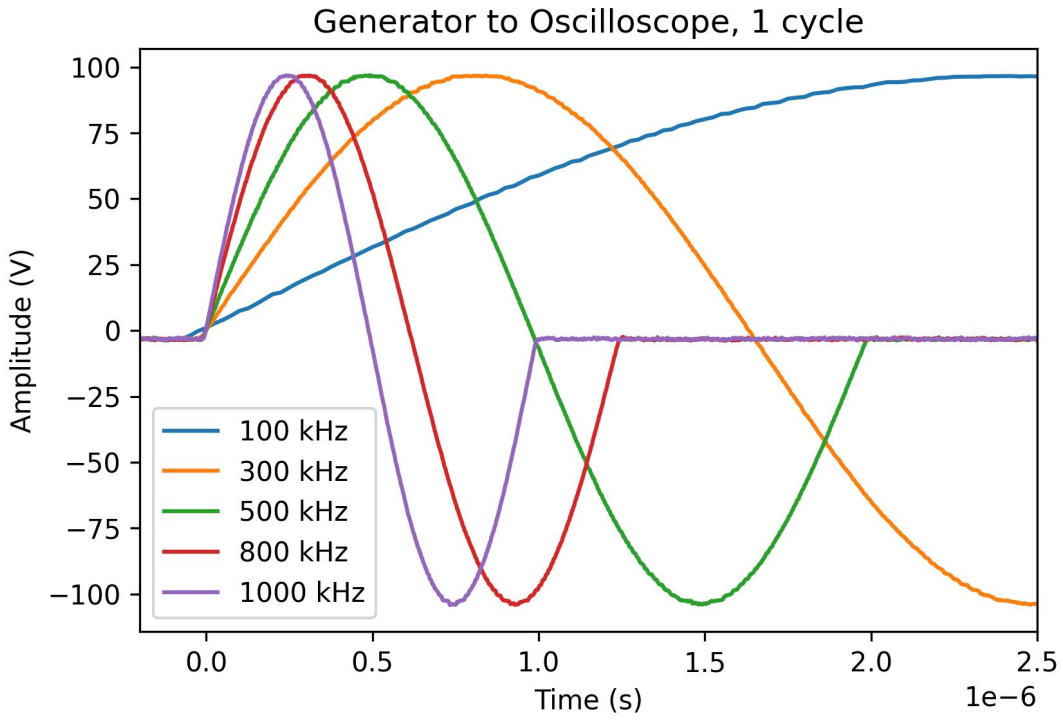

Figure 2.7: Single-cycle pulses transmitted directly from the generator to the oscilloscope. Each pulse has a different period. A small time window (0 to 2.5x10^{-6} s) of the raw data is shown to illustrate the differences in periods.

frequencies ranging from 100 kHz to 1 MHz, in accordance with the desired frequency that we set on the waveform generator. This result also confirms that our oscilloscope can decipher signals with different frequencies. That is, the oscilloscope is able to measure voltage changes and record the time at which each voltage occurs. Furthermore, we use the raw data shown in Figure 2.7 as a reference of what changing the input frequency looks like in the time domain. To evaluate this data in frequency space, in Figure 2.8, we present the FFT spectra of the raw data obtained from transmitting a series of single-cycle pulses over the range of 100-1000 kHz. All FFT spectra in section 2.1.3 were calculated using the entire raw data set. Each pulse has a distinct central frequency and all central frequencies are in agreement with their respective input frequencies within their respective uncertainties.

The results presented in Figure 2.8 support the conclusion that an FFT spectrum allows for the qualitative resolution of single-cycle pulses. It is worth noting that for all FFT data presented in this thesis, intensities have been normalized. That is, all intensities have been divided by their respective maximum intensity to yield values ranging from 0 to 1. The goal of transforming our raw data into frequency space is to compare peak shifts, not to analyze absolute intensities. This becomes especially relevant in Chapter 3 because consideration of the factors affecting amplitude was outside the scope of this thesis. For example, the amount of couplant, the temperature of the couplant and the tightness of the bar clamp are all factors that we expect to impact elastic wave transmission but were not controlled for.

When compared to our motivation data in Figure 1.4, we conclude that the FFT algorithm is not to blame for the apparent frequency conversion (i.e. when the frequency content of the measured waveform is in disagreement with the input frequency). Here, the resolution is fine enough to distinguish between elastic waves with frequencies of

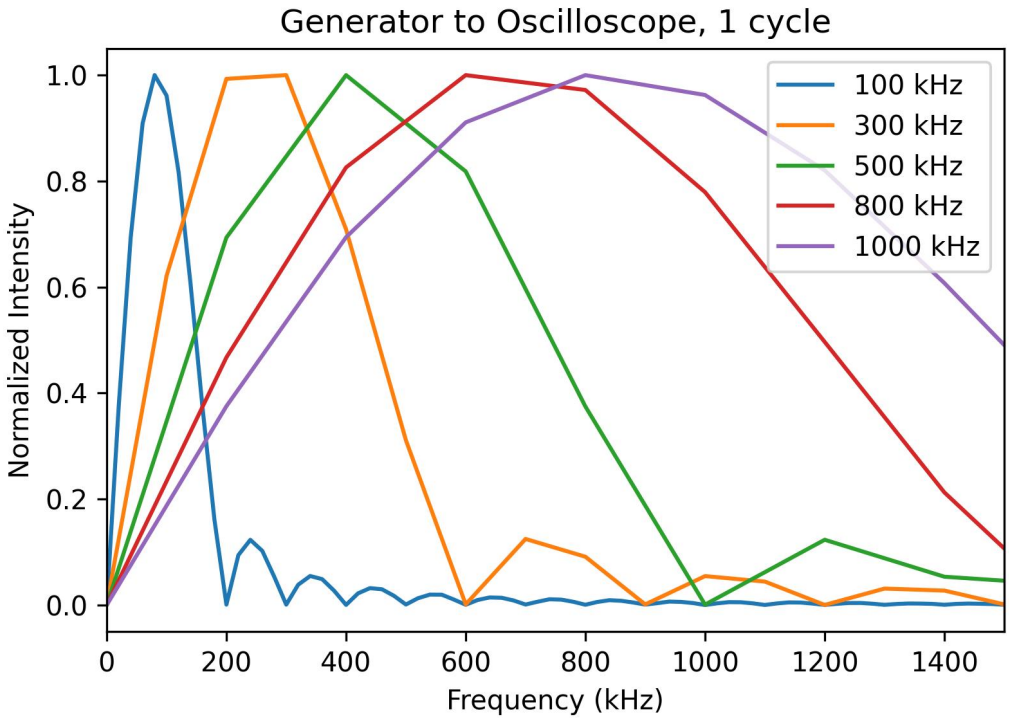

Figure 2.8: FFT spectra of single-cycle pulses transmitted directly from the generator to the oscilloscope. Each spectrum has a different central frequency (80±50 kHz, 300±200 kHz, 400±300 kHz, 600±500 kHz, 800±500 kHz). FFT spectra were calculated using the full raw data sets.

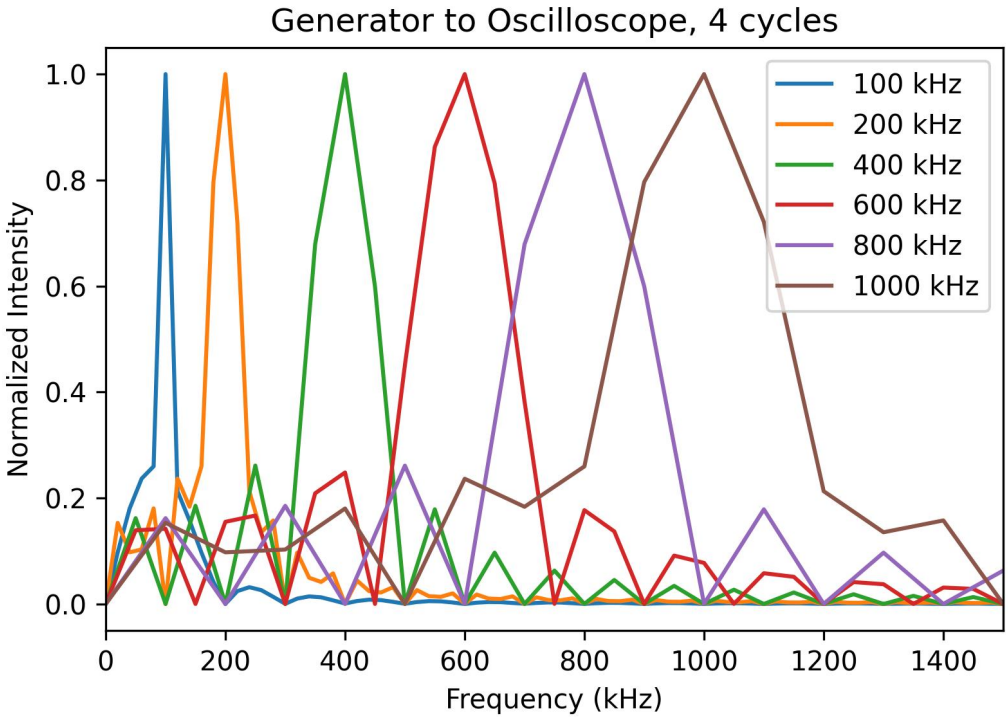

Figure 2.9: FFT spectra of 4-cycle pulses transmitted directly from the generator to the oscilloscope. Each spectrum has a different central frequency (100±20 kHz, 200±30 kHz, 400±50 kHz, 600±100 kHz, 800±100 kHz, and 1000±200 kHz) that is in agreement with the input frequency (legend). FFT spectra were calculated using the full raw data sets.

100 kHz, 300 kHz, 500 kHz, 800 kHz, and 1 MHz. However, this resolution is potentially too broad to provide meaningful quantitative results, especially as frequency increases. This plot is crucial in illustrating the limitation of using FFT in our analysis. As illustrated in Figure 2.8, peak widths increase as input frequency increases, meaning our ability to sharply resolve peak locations decreases with frequency.

We repeat the process of transmitting a series of pulses over the range of 100-1000 kHz, now for 4-cycle pulses and continuous pulses. Figures 2.9 and 2.10 show the FFT spectra of 4-cycle pulses and continuous pulses, respectively. When we compare these results to those in Figure 2.8, we conclude that increasing the number of cycles

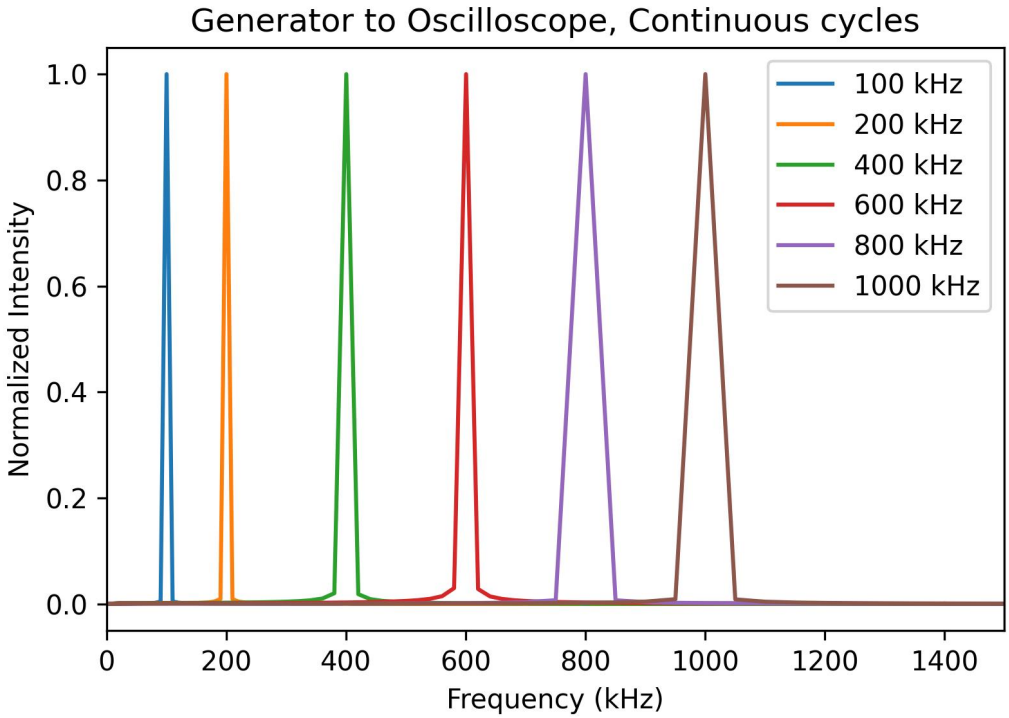

Figure 2.10: FFT spectra of continuous-cycle pulses transmitted directly from the generator to the oscilloscope. Each spectrum has a different central frequency (100±4 kHz, 200±4 kHz, 400±10 kHz, 600±10 kHz, 800±20 kHz, and 1000±20 kHz) that is in agreement with the input frequency (legend). FFT spectra were calculated using the full raw data sets.

in the signal results in narrower peaks. The central frequencies in Figures 2.9 and 2.10 are all in accordance with their respective input frequencies. In turn, increasing the number of cycles improves our ability to resolve peak locations which means an improvement in our ability to obtain reliable quantitative frequency information. Figure 2.10 shows the FFT spectra of continuous pulses at various input frequencies. This plot shows how our frequency resolution is significantly improved (peak width, not df) when the signal interpreted by the FFT algorithm possesses more cycles per pulse. The degree to which peak widths change with frequency and the number of cycles was discussed in detail in section 2.1.2.

The results presented in this section give us confidence in our equipment's ability to transmit and receive signals of desired frequencies. That is, our key takeaway from this chapter is that malfunctions in our waveform generator, oscilloscope and coaxial cables are not responsible for the frequency shifts presented in our motivation data. It should be reiterated that the width of FFT peaks increase as input frequency increases, meaning our ability to sharply resolve peak locations decreases with frequency. This proves to be an inherent property of applying the FFT algorithm. We conclude that when attempting to make precise frequency measurements of single-cycle pulses, it is better to fit the pulse with a sine function instead of simply calculating the FFT of such narrow pulses.

The resolution of the FFT is a limitation in this study. With peaks spanning several hundred kilohertz, it is difficult to accurately measure the frequency of the single-cycle pulses using FFT analysis. Moreover, this study focuses largely on single-cycle pulses, rendering it impossible to measure narrow peaks. Recalling the single-cycle FFT presented in Figure 2.8, even under ideal conditions (no transducers and sample material to distort the signal), the high frequency (1 MHz) FTT peaks resemble normal distributions. A single-cycle wave consists of a wide range of frequencies required to create the sharp stop and start regions of the wave. Therefore, an FFT spectrum is not a useful tool to measure the absolute frequency of a single-cycle pulse. However, comparing FFT spectra is useful for checking if two pulses have the same frequency components. This is especially important when the degree of likeness is not visually apparent in the time domain. This thesis relies on the use of FFT spectra to provide quantitative measurements of frequency content through peak positions and widths. The FFT is an effective tool for quantifying single-cycle frequency changes. However, large peak widths make it difficult to track small changes in frequency. Luckily for us, the single-cycle FFT is very effective when it comes to comparing the

frequency content of pulses. This point becomes increasingly evident and important in section 3.1 when we examine transducer responses in coupled conditions.

2.2 Uncoupled Transducers

2.2.1 Introduction

In section 2.1, we established that the waveform generator, oscilloscope and coaxial cables are functional. Thus, the question of what is to blame for the frequency shift described in Chapter 1 remains unanswered. In an attempt to answer this question, we proceed with the next progression in the step-wise process of building toward the Transient Wave Dynamic Acousto-elastic Testing setup. This next progression is the introduction of transducers. In section 2.2, we test transducers in uncoupled conditions to assess their individual capacity to produce pulses with desired properties.

2.2.2 Methods

The goal of the experiments presented in section 2.2 is to assess our transducer's ability to produce waves corresponding to the parameters set on the function generator. In short, this experiment serves to isolate the ultrasonic transducers, assess their ability to generate a desired signal and provide a baseline for expected transducer outputs in uncoupled conditions. To do so, we employ a well-recognized laser vibrometry technique [25, 31, 26]. In this technique, an optical beam from a laser interferometer arrives perpendicular to the transducer face. The transducer is excited by electrical pulses from the waveform generator, causing the transducer face to vibrate. The beam reflects off the oscillating transducer surface and travels back to

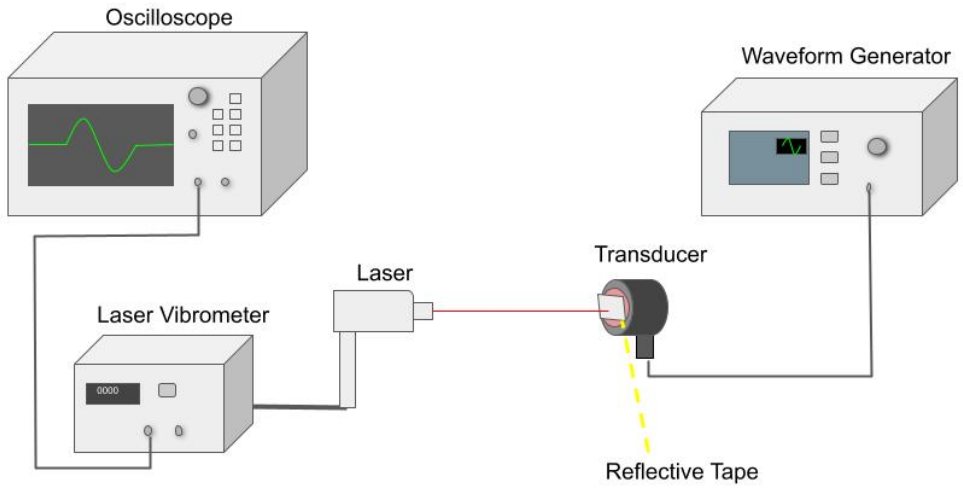

Figure 2.11: Experimental setup for testing individual transducers using a laser vibrometer.

the interferometer where its phase shift is measured [25]. A mathematical description of this process is outlined in [25] on page 162. This technique has been employed on ultrasonic transducers to assess their ability to produce and sense elastic waves with various frequencies [25] and to measure transducer sensitivity [31]. Furthermore, at the University of Auckland's Physical Acoustic Laboratory, the method of pairing laser vibrometry and ultrasonics is commonplace. For instance, they use this technique to measure the vibrations of rock surfaces, induced by ultrasonic transducers, to extract elastic properties [26].

The experimental setup we employ in this chapter is depicted in Figure 2.11. A coaxial cable connects the *velocity* output port on the laser vibrometer (Polytec CLV-2534 Laser Vibrometer) to an input channel on the oscilloscope. The *Sync* port on the waveform generator is connected to the oscilloscope via a coaxial cable to the *Ext trig in* port. Next, the waveform generator is connected to the ultrasonic transducer.

The transducer is fixed to a stationary block on the tabletop using a bar clamp, which allows us to align the laser with the transducer surface. The transducer is clamped by its sides such that the oscillating surface is uncoupled. The block and clamp have been omitted from Figure 2.11 for clarity. We apply reflective tape to the face of the ultrasonic transducer and set the desired parameters on the waveform generator. We position the optical laser beam at the center of the transducer face using stepping motor controls. Finally, we record the oscillations on our oscilloscope. This setup allows us to examine whether the parameters we set on the function generator are truly impacting the properties of the elastic waves produced by our transducers. The three parameters we adjust in this experiment are frequency, number of cycles, and transducer type (P-wave and S-wave). We begin with a series of single-cycle pulses over the range of 50-200 kHz.

Ultrasonic Transducers

This study uses a variety of Olympus ultrasonic contact transducers fitted with right BNC connectors (see Figure 2.12). These transducers include S-wave transducers and P-wave transducers. The Olympus V153 is an S-wave ultrasonic contact transducer with a frequency of 1 MHz and a diameter of 0.5 inches (1.27 cm). The Olympus V103 is a P-wave ultrasonic contact transducer with a frequency of 1 MHz and a diameter of 0.5 inches (1.27 cm). With regards to the pump-probe configuration discussed in Chapter 1 (see Figure 1.3), the aforementioned transducers used in this thesis can be categorized as probe transducers, due to their relatively high frequency. For context, the low-frequency transducers used by Newman (2020) to pump energy into the system and perturb the samples were the Olympus V1548 S-wave ultrasonic contact transducers, with a frequency of 0.1 MHz and a 1-inch (2.54 cm) diameter.

Figure 2.12: Olympus ultrasonic contact transducers. Our P-wave and S-wave transducers are identical in appearance but distinguishable by serial numbers.

These low-frequency transducers operate at one-tenth the frequency of the probe transducers used in this thesis.

According to the Ultrasonic Transducers Technical Notes released by Olympus [19], the manufacturer, our transducers are single-element transducers. They are designed for direct contact with the object of interest and are built to perform in industrial settings. The main components of these contact transducers are the piezoelectric element, the backing, and the wear plate [19]. A wear plate has several functions, such as increasing the lifespan of the device and offering wear resistance [19]. According to Olympus (2019), P-wave transducers can be used for "straight beam flaw detection and thickness gaging, detection and sizing of delaminations, material characterization and sound velocity measurements, inspection of plates, billets, bars, forgings, castings, extrusions, and a wide variety of other metallic and nonmetallic components" (p. 8). On the other hand, our S-wave transducers are designed for "shear wave velocity measurements, calculation of Young's modulus of elasticity and shear modulus, and characterization of material grain structure" (p. 17).

It should be noted that the method we employ in this chapter to test individual

transducers does not operate in the same frequency range as the transducers themselves. The probe transducers used here are 1 MHz transducers, meaning they operate optimally within a bandwidth centred at 1 MHz. Conversely, our laser vibrometer is unable to resolve frequencies above approximately 200 kHz. Therefore, we examine these transducers over the range 50-200 kHz. We acknowledge that this frequency range is sub-optimal. However, if the transducers are operational at frequencies on the edge of their bandwidth, it is assumed that their performance would only improve if they were evaluated at optimal frequencies.

2.2.3 Results

This experiment isolates the ultrasonic transducers to assess their ability to generate a desired signal and provide a baseline for expected transducer outputs in uncoupled conditions. The three variables discussed in this section are frequency, number of cycles, and transducer type (P-wave and S-wave). We begin with a series of single-cycle pulses over the range of 50-200 kHz, transmitted using an S-transducer. These time-domain signals are presented in Figure 2.13A, with a small section of the raw waveforms shaded in grey.

From Figure 2.13A, we learn that our S-transducers can produce pulses with varying periods. We use the raw data shown in 2.13A as a baseline for what our ultrasonic pulses look like without the presence of a solid. To evaluate this data in frequency space, in Figure 2.13B, we present the FFT spectra of the entire raw data shown above in Figure 2.13A. Throughout this thesis, we calculate our FFT spectra using the entire raw data set to maintain consistency and maximize our frequency resolution. Due to limitations in the laser vibrometer setup, which we've discussed previously, we examine FFT spectra calculated using only a section of the raw data to exclude

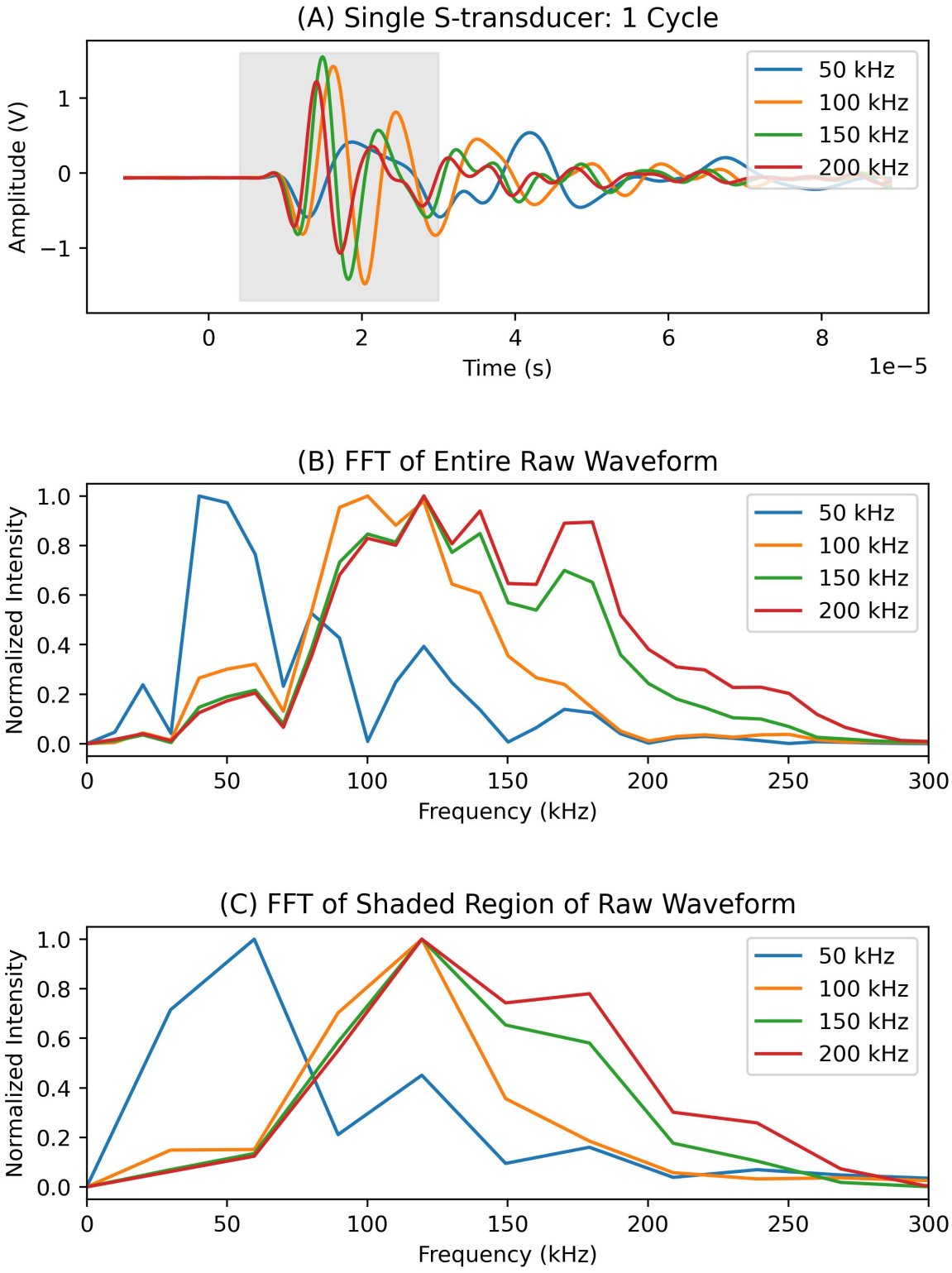

Figure 2.13: Uncoupled S-transducers generating 1-cycle pulses. (A) Entire raw waveforms with a shaded region. (B) FFT spectra of the entire raw waveform shown in (A), df=10 kHz. Central frequencies are 40±20 kHz, 100±40 kHz, 120±50 kHz and 120±60 kHz. (C) FFT spectra of raw data were calculated using the data in the shaded region in (A), df=30 kHz. Central frequencies are 60±50 kHz, 120±40 kHz, 120±50 kHz, 120±60 kHz.

the artifacts at the end of our signals. In Figure 2.13C, we present the FFT spectra calculated using only the grey shaded region in Figure 2.13A. As expected, reducing the time window over which we calculate our FFT spectra worsens our frequency resolution (from 10 kHz to 30 kHz) because of the inverse relationship between time and frequency sampling (recall Figure 2.2). Here, we uncover that it is unreasonable to place significant weight on the exact location of our central maxima, as they are heavily dependent on input parameters, such as the duration and location of our time window. This point is discussed further, surrounding the following figure (2.14). In Figures 2.13B and 2.13C, each of the central frequencies are in accordance with their respective input frequencies within the range of uncertainty. This suggests that our S-transducers have the ability to act as ultrasonic sources, which can generate single-cycle pulses over the range of 50 kHz-200 kHz. Although, in both cases, the latter two spectra have the same central frequency.

In Figure 2.14, we illustrate how the choice of time window in the time domain has a significant impact on the FFT spectrum. As previously stated, the exact location of our central maximum is heavily dependent on the duration and location of our time window. In changing the time window used to calculate the FFT, the resulting spectra possess different central frequencies, different resolutions and vastly different shapes. The central frequency of the full waveform is 120 kHz, but after cropping the waveform to include only the shaded region shown in Figure 2.14A, the central frequency shifted to 182 kHz. The central frequency of the cropped waveform (shaded region) is in closer agreement with the input frequency of 200 kHz, however, the frequency spacing (df) has increased significantly, from 10 kHz to 182 kHz. This highlights an important point: central maxima can only exist at multiples of df, therefore, reporting a frequency shift as a result of changing the time window is meaningless, as it reflects the lack of resolution and not transducer behaviour. For

this reason, and to maintain consistency and maximize the frequency resolution, all FFT spectra we present in this thesis are calculated using the entire raw waveform, unless stated otherwise. Hence, inconsistencies in the frequency resolution (df) are attributed to saving the data using different time windows during the acquisition process and not signal processing.

Due to a malfunction with the oscilloscope's data acquisition process involving the USB port, our laser vibrometer data for single-cycle pulses sent from P-transducers was lost. Therefore, we cannot comment on our P-transducers ability to send single-cycle pulses in uncoupled conditions. However, in Figure 2.15, we examine S-transducers and P-transducers by presenting our data obtained from transmitting a series of 10-cycle pulses over the range of 50-200 kHz.

Here, we independently examine a pair of S-transducers (Figure 2.15A and B) and a pair P-transducers (Figure 2.15C and D). Once again, the results in Figure 2.15 reaffirm our previous conclusion that FFT peaks narrow when the number of cycles is increased. In the case of all four transducers, the central frequencies of the frequency spectra are in accordance with the input frequencies shown in the legends. Critically, we can conclude that the inability to control output frequency, described in Chapter 1, is not an inherent property of our transducers. This is a key finding, as it allows us to proceed with the confidence that our transducers can generate pulses with desired properties.

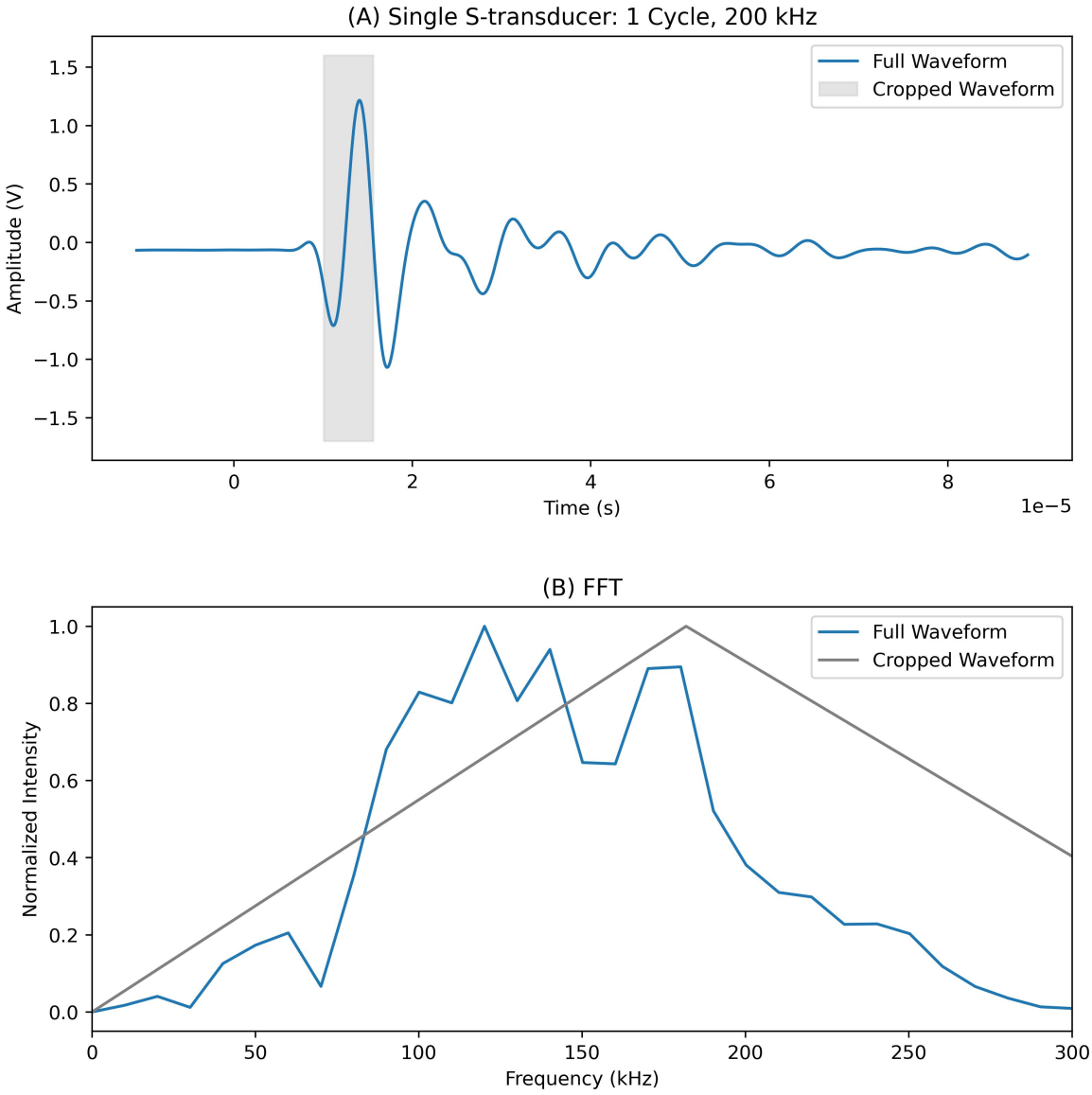

Figure 2.14: Time window selection affecting FFT spectrum and central frequency. (A) Raw data of a single-cycle 200 kHz pulse from S-transducers (blue) and a cropped region of the first cycle in the pulse (grey). (B) FFT of the full waveform from above (blue) and the cropped region (grey). Cropping the waveform causes the central frequency to shift from 120 kHz to 182 kHz, but it increases the frequency spacing (df) from 10 kHz to 182 kHz, significantly worsening the resolution.

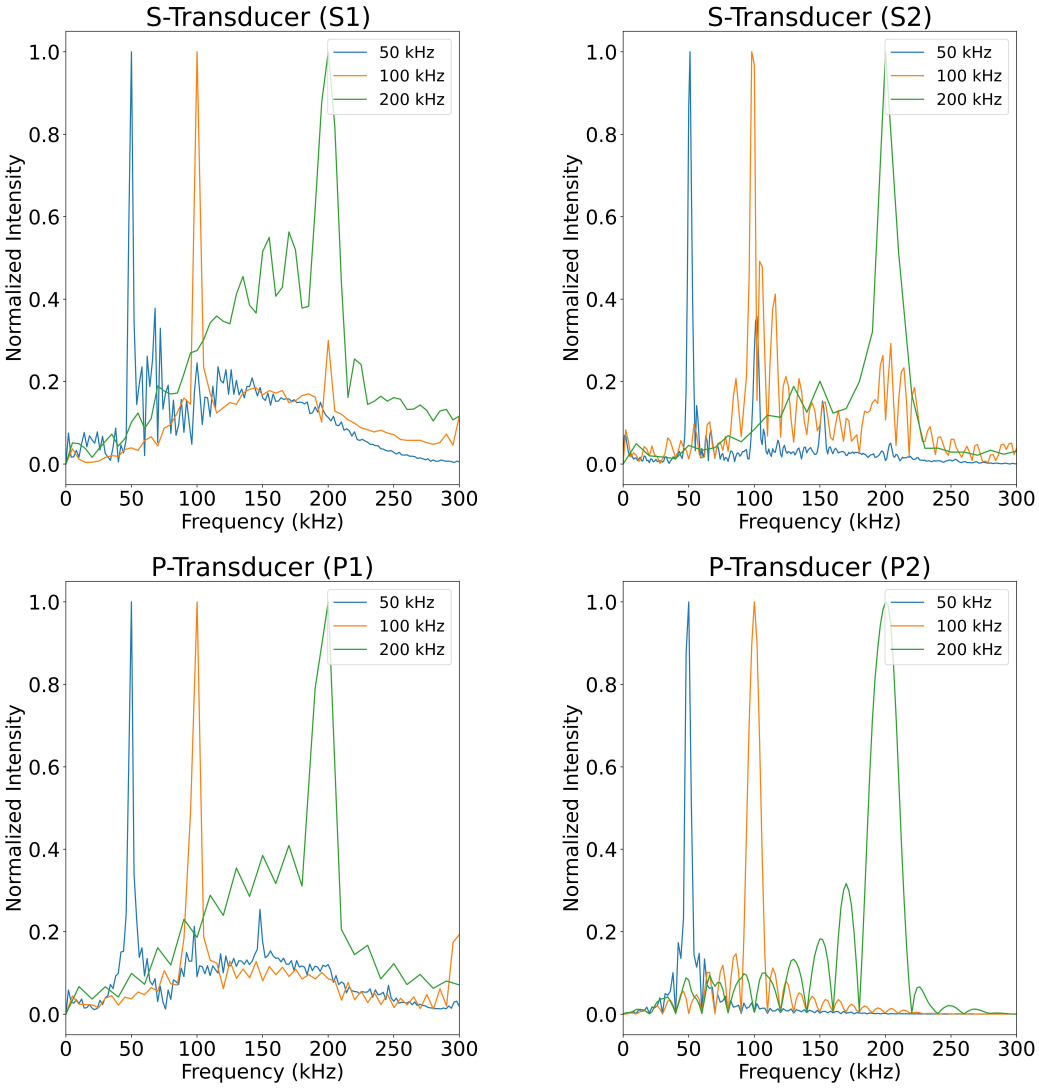

Figure 2.15: FFT spectra of 10-cycle pulses generated by uncoupled (top) S-transducers and (bottom) P-transducers using the laser vibrometer setup. FFT spectra were calculated using the entire raw data sets. For all four transducers, the central frequencies of all pulses are in accordance with the input frequencies (S1: 50±2 kHz, 100±4 kHz and 200±10 kHz; S2: 50±3 kHz, 100±4 kHz and 200±10 kHz; P1: 50±3 kHz, 100±4 kHz and 200±10 kHz; P2: 50±3 kHz, 100±5 kHz and 200±10 kHz).

Chapter 3

Coupled Transducers

3.1 Introduction

In this chapter, we build upon the results obtained in previous chapters to approach the implementation of a Transient Wave Dynamic Acousto-elastic Testing (TW-DAET) setup. In Chapter 2, we established that the waveform generator, oscilloscope and coaxial cables are functional and are, therefore, not to blame for the frequency shift described in Chapter 1. Moreover, we tested transducers in uncoupled conditions and established that individual transducers can produce single-cycle pulses with desired properties. Now, we take one more step toward the TW-DAET set up to investigate whether the act of coupling our transducers to a sample material causes frequency conversion (i.e. the frequency content of the measured waveform is in disagreement with the input frequency). Based on the results presented in previous sections, this essentially isolates the effect that coupling our transducers to a sample material has on the output signal. In this chapter, we investigate this effect using S-wave transducers and P-wave transducers.

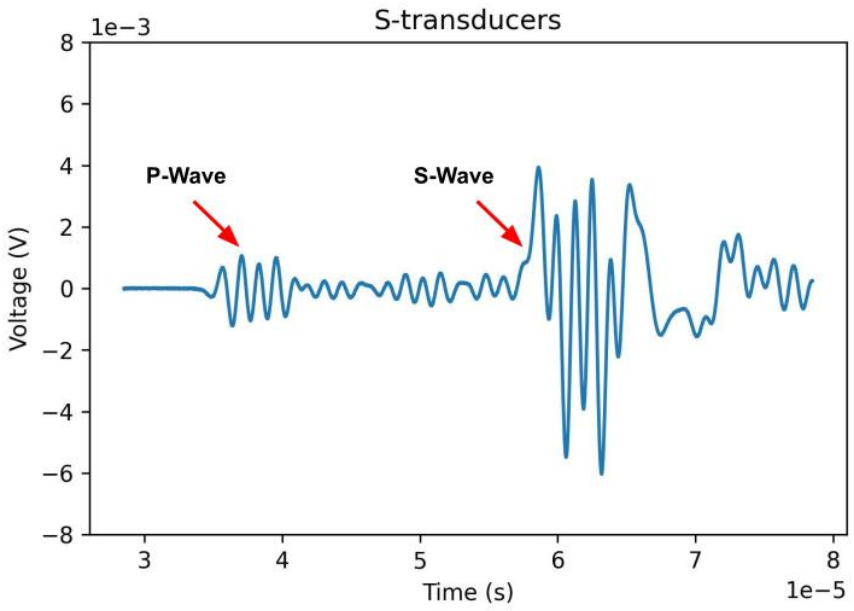

Figure 3.1: Expected signal resulting from S-transducers, highlighting the production of a parasitic P-wave.

With P-wave transducers (P-transducers), the transducer surface moves in the normal direction to produce compressional waves. The surface of an S-wave transducer (S-transducer) primarily exhibits lateral motion, which generates S-waves. However, due to edge effects, the surface of an S-transducer inevitably undergoes translation in the normal direction, resulting in the production of a parasitic P-wave [32], as shown in Figure 3.1. P-waves are known to have significantly less energy than S-waves. They also have higher velocities, so a parasitic P-wave arrives before its corresponding S-wave. In section 4.2, we propose a series of experiments to investigate these edge effects and further understand the origin of parasitic P-waves. Interestingly, recalling the transducer responses presented in Figure 2.13A, we do not observe parasitic P-waves when S-wave transducers are tested individually in uncoupled conditions.

Parasitic P-waves are relevant to this thesis because Newman (2020) tracked the

parasitic P-wave portion of the single-cycle probe wave generated and sensed by S-transducers, leading to the result which motivated this thesis. Therefore, in this chapter, we investigate our ability to control the frequency of both the intended S-wave and the parasitic P-wave when our S-transducers are coupled with various materials.

3.2 Methods

In this chapter, we employ a two-transducer pulse transmission technique [1, 32]. This technique uses two transducers aligned on opposite ends of the sample, as illustrated in Figure 3.2. One transducer acts as the source, and the other acts as the receiver. The source transducer produces an ultrasonic elastic wave which propagates through the sample and is then sensed by the receiver on the other end. S-transducers generate transverse waves which displace particles parallel to the transducer's polarity [32]. According to Olympus, the transducer manufacturer, their S-transducers are polarized in line with their right-angle BNC connectors. Therefore, we position our transducers such that the source and receiver BNC connectors are aligned to ensure their polarity directions are the same. The transducers are bonded to the surface of the sample using honey and held in place using a bar clamp.

As discussed in Chapter 1, using ultrasonic transducers to measure non-linearity is important in many fields. Therefore, this study aims to gain an understanding of how transducers behave when coupled with various materials, such as homogeneous cement (linear), inhomogeneous cement and sandstone (nonlinear). The dimensions of the sample materials used in this chapter are presented in Table 4.1. More information on the synthesis of these cement samples is available on page 25 of [17].

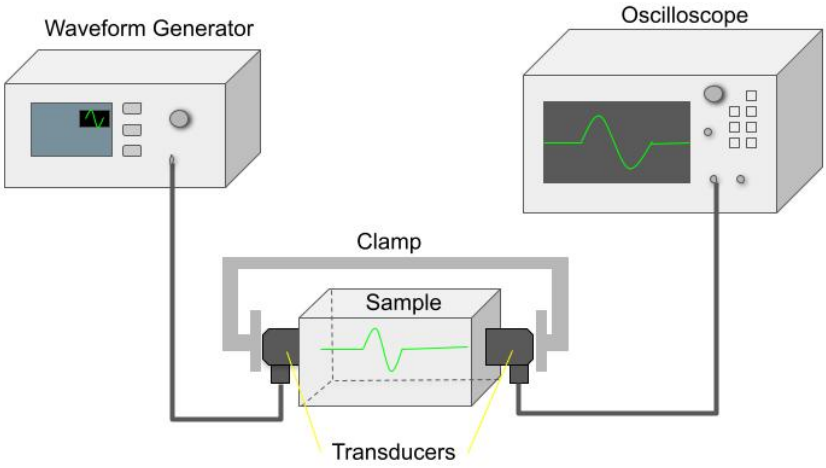

Figure 3.2: Experimental setup of two-transducer pulse transmission technique.

Sample Material	**x** (mm)	**y** (mm)	**z** (mm)
Homogeneous Cement	183	117	51.8
Cement with Copper Wires	182	115	39.9
Sandstone	101	101	52.4

Table 3.1: Dimensions of sample materials.

3.3 Results

3.3.1 No Sample

P-Transducers We begin by coupling two P-transducers together without introducing a sample material between the pair. Here, our P-transducers are bonded together with honey and clamped together with a bar clamp. In Figure 3.3A, we present our raw data obtained from transmitting a series of single-cycle pulses over the range of 100 kHz to 1 MHz. Here, we show the first 3 microseconds of each pulse to highlight the differences in periods.

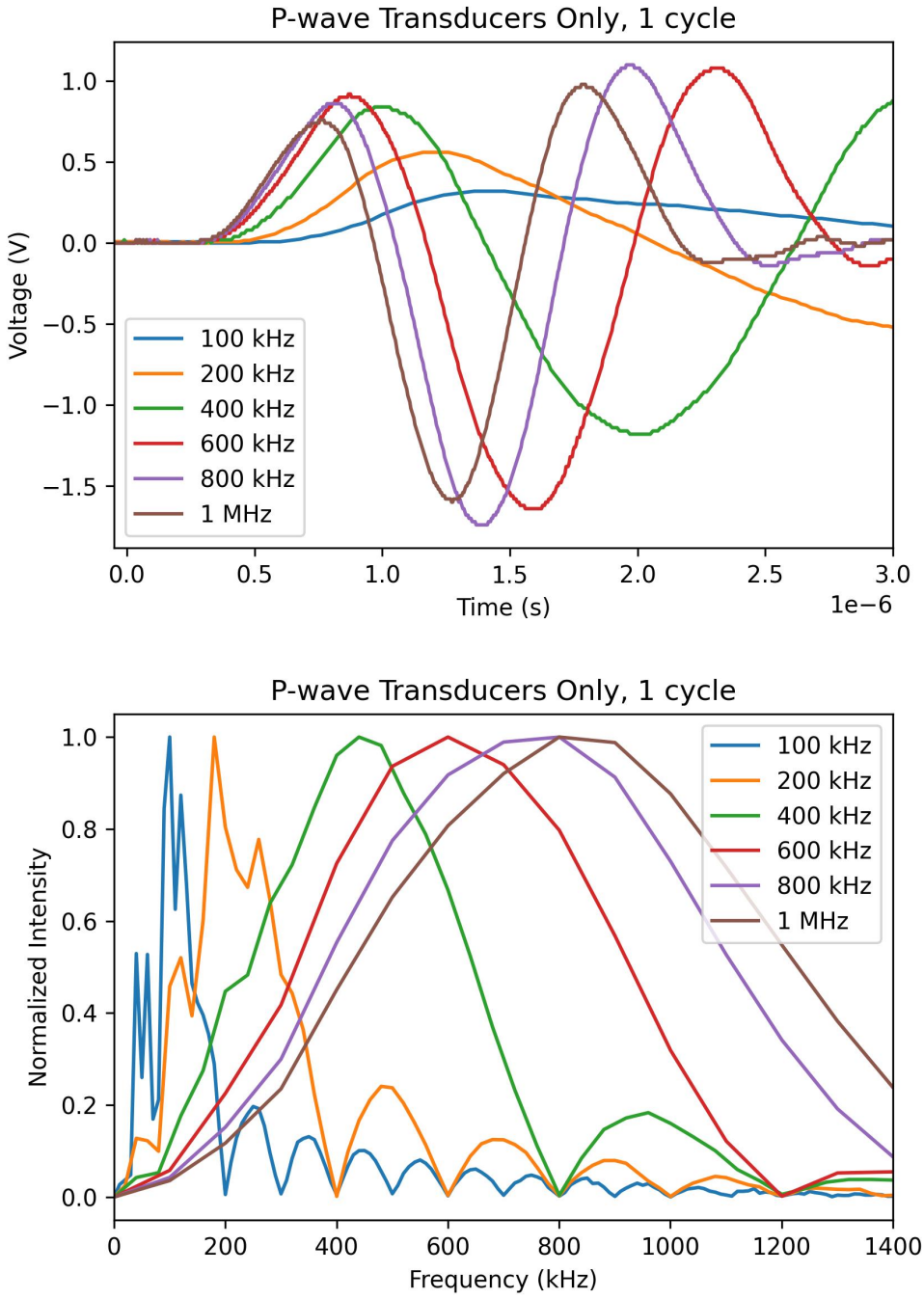

Figure 3.3: Single-cycle pulses from P-wave transducers coupled together with no sample. (A) A small time window (0 to $3x10^{-6}$ s) of the raw data is shown to illustrate the differences in periods. (B) FFT spectra calculated from entire raw waveforms. Central frequencies are in accordance with input frequencies (see legend): 100±50 kHz, 180±100 kHz, 440±200 kHz, 600±300 kHz, 800±400 kHz, 800±400 kHz.

In Chapter 2, we verified that our P-transducers are capable of **producing** ultrasonic pulses of different frequencies. The data presented in Figure 3.3A allows us to assess our P-transducers' ability to **sense** ultrasound pulses with different frequencies. Upon visual analysis, it is apparent that the single-cycle pulses in Figure 3.3A possess different periods. This confirms that when acting as the receiver, our P-transducers do not preferentially sense certain frequencies, as long as amplitude information is ignored. Furthermore, we use the raw data shown in 3.3A as a baseline for what our ultrasonic pulses look like when they are both generated and sensed by P-transducers (clamped together), and have passed through a thin ($\ll \lambda$) intermediate layer of honey without the presence of a solid. To evaluate this data in frequency space, in Figure 3.3B, we present the FFT spectra of the raw data over the range 100 kHz to 1 MHz. In Figure 3.3B, it is apparent that each pulse possesses a different frequency spectrum, many of which have different central frequencies. The central frequency of the 100 kHz pulse, the 600 kHz pulse and the 800 kHz pulse are exactly in accordance with the input frequency, while the others are in accordance within their uncertainty ranges. Notably, both the 800 kHz pulse and 1 MHz pulse have the same central frequency. In all, all pulses possess different periods and most possess different central frequencies. This suggests that our P-transducers have the ability to act as receivers which can sense single-cycle pulses over the examined range.

S-Transducers We repeat the analysis conducted above, but now using S-transducers. We begin by coupling the two S-transducers together without introducing a sample material between them. Here, a pair of S-transducers are bonded together with honey and clamped together with a bar clamp. In Figure 3.4A, we present our raw data obtained from transmitting a series of single-cycle pulses over the range of 200 kHz-1 MHz. In this figure, we show only the first 3.5 microseconds of each pulse to highlight

the differences in periods. However, the FFT spectra in Figure 3.4B were calculated using the entire raw waveforms.

In Chapter 2, we verified that our S-transducers are capable of **producing** single-cycle pulses of different frequencies. Assuming that our transmission is still sound, we incorporate a reception component to assess our S-transducers' ability to **sense** ultrasonic pulses with different frequencies. Upon visual analysis, it is apparent that the single-cycle pulses in Figure 3.4A possess different periods. This confirms that when acting as the receiver, our S-transducers do not preferentially sense certain frequencies. Further, we do not observe parasitic P-waves when S-wave transducers are coupled together using honey and a bar clamp. This is likely because the travel-time difference between the parasitic P-wave and the S-wave is small. We use the raw data shown in Figure 3.4A as a baseline for what our ultrasonic pulses look like when they are both generated and sensed by S-transducers. Moreover, this baseline is crucial in establishing how pulse transmission is affected by clamping our transducers together and travelling through a thin ($\ll \lambda$) intermediate layer of honey without the presence of a solid. We tested both configurations for the order of the transducers (e.g. which one is transmitting and which one is receiving) and found that, aside from amplitude, the configuration does not affect the signal. To evaluate this data in frequency space, in Figure 3.4B, we present the FFT spectra of the entire raw waveforms shown partially in Figure 3.4A over the range 200 kHz to 1 MHz.

In Figure 3.4B, it is apparent that each pulse possesses a different frequency spectrum. Given that each pulse in the time domain possesses a different period, this is expected. It should be noted that all FFT spectra were calculated using the entire raw data set. Several pulses have distinct central frequencies. The central frequencies

A

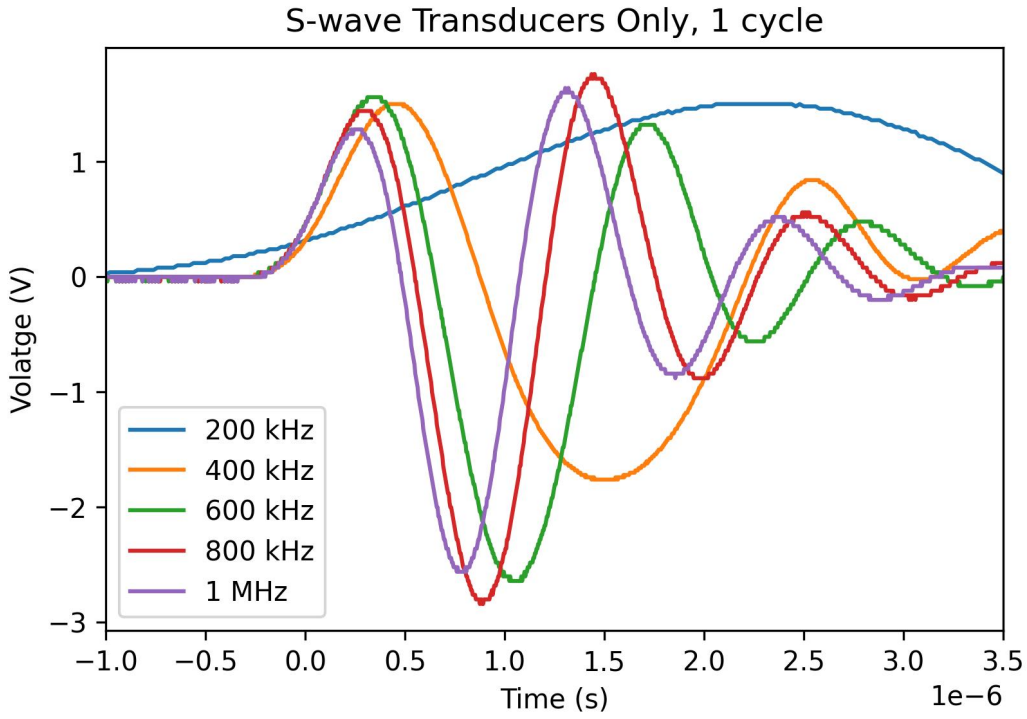

B

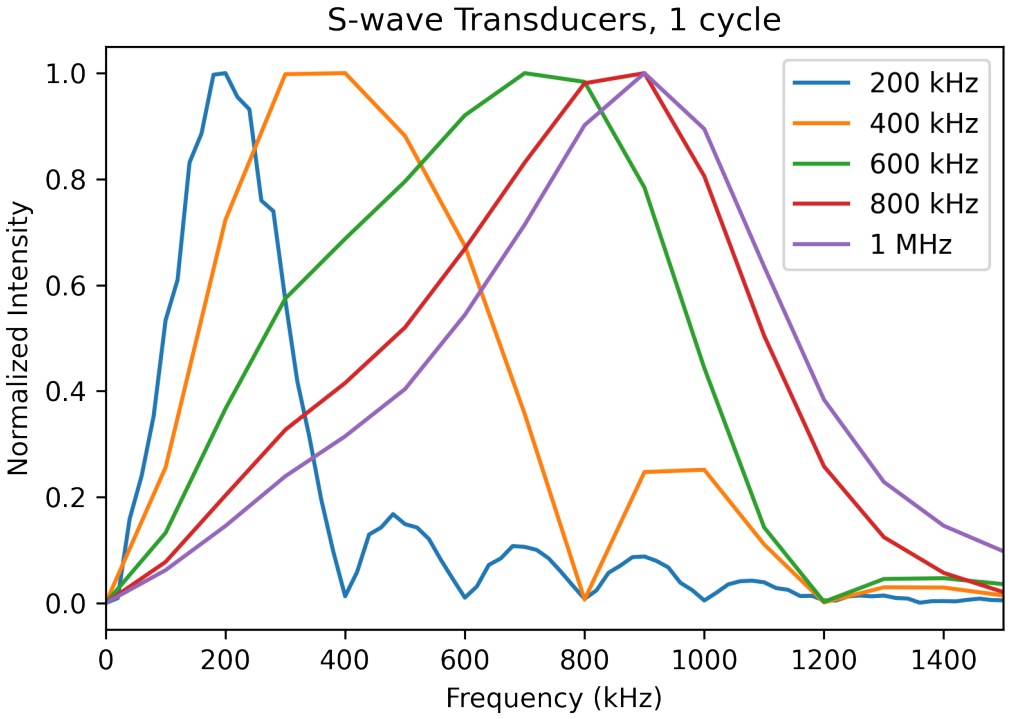

Figure 3.4: Single-cycle pulses from S-wave transducers coupled together with no sample. (A) A small time window (-1x10^{-6} s to 3.5x10^{-6} s) of the raw data is shown to illustrate the differences in periods. (B) FFT spectra were calculated from entire raw waveforms. Central frequencies are in accordance with input frequencies (see legend): 200±50 kHz, 400±200 kHz, 700±300 kHz, 900±300 kHz and 900±300 kHz.

of the 200 kHz and 400 kHz pulses are exactly in accordance with the input frequencies, while the others are in accordance within their uncertainty ranges. Notably, just as we found with P-transducers in Figure 3.3B, both the 800 kHz pulse and 1 MHz pulse have the same central frequency. Unexpectedly, it appears that for 1 MHz transducers, central frequencies are more accurate at low frequencies. However, these peak locations are highly dependant on the time-window and segment of data used to calculate the FFT and therefore may not be indicative of transducer behaviour. This could be investigated further by fitting the raw data with a function, as shown in section 2.1.2 (Figure 2.4). We do not implement this curve-fitting approach throughout this thesis because our FFT spectra provide sufficient information to draw conclusions about frequency content without the need for precise frequency measurements. This confirms that our S-transducers have the ability to act as receivers which can sense single-cycle pulses over the examined range. The results presented in Figure 3.4B support the conclusion that the frequency discrepancy described in Chapter 1 is not a result of our coupling methods. In other words, the bar clamp and honey used to couple the transducers together do not introduce frequency conversion.

3.3.2 Linear Sample: Homogeneous Cement

S-Transducers Next, we build upon the results obtained previously to approach the implementation of a Transient Wave Dynamic Acousto-elastic Testing (TW-DAET) setup. We do so by introducing sample materials between our transducer pair to investigate whether the act of coupling our transducers to a sample material causes frequency conversion. We begin by using a sample of homogeneous cement, which is known to be linearly elastic [17]. We transmit a series of single-cycle pulses ranging from 500 kHz to 1.2 MHz. It should be noted that all cement samples examined in

this thesis are the exact samples used by Newman (2020). It must also be noted that signals have been translated in time to highlight alignment and likeness in the periods. Therefore, the arrival times in our time-domain figures do not reflect the true arrival times. We examine the S-wave signal and the parasitic P-wave component of the signal separately.

Firstly, the parasitic P-wave component of the signal is shown in Figure 3.5A. To evaluate this data in frequency space, in Figure 3.5B, we present the FFT spectra of the entire raw data set shown in Figure 3.5A. Here, the most striking observation to emerge is that the frequency of the elastic waves did not change as the frequency parameter was changed on the generator. Just as we described in Chapter 1 (see Figure 1.4), the central frequency of our pulses do not match the input parameters shown in the legend. Furthermore, all signals possess the same central frequency of 400 kHz. This result allows us to conclude that the frequency of the parasitic P-wave component of a single-cycle pulse transmitted through homogeneous cement using S-transducers is independent of the input parameters over the examined frequency range. Critically, this finding allows us to conclude that the frequency conversion described in Chapter 1 is not a result of the cement with an embedded network of evenly spaced (5mm) copper wires possessing frequency conversion properties.

Next, the S-wave component of the signal is shown in Figure 3.6A. To evaluate this data in frequency space, in Figure 3.6B, we present the FFT spectra of the entire raw data, shown partially in Figure 3.6A. Once again, we observe that the frequency of the elastic waves did not change as the frequency parameter was changed on the generator. The central frequencies of our pulses do not match the input parameters shown in the legend. Furthermore, all signals possess the same central frequency of 280 kHz. This result allows us to conclude that the frequency of both the S-wave and the parasitic

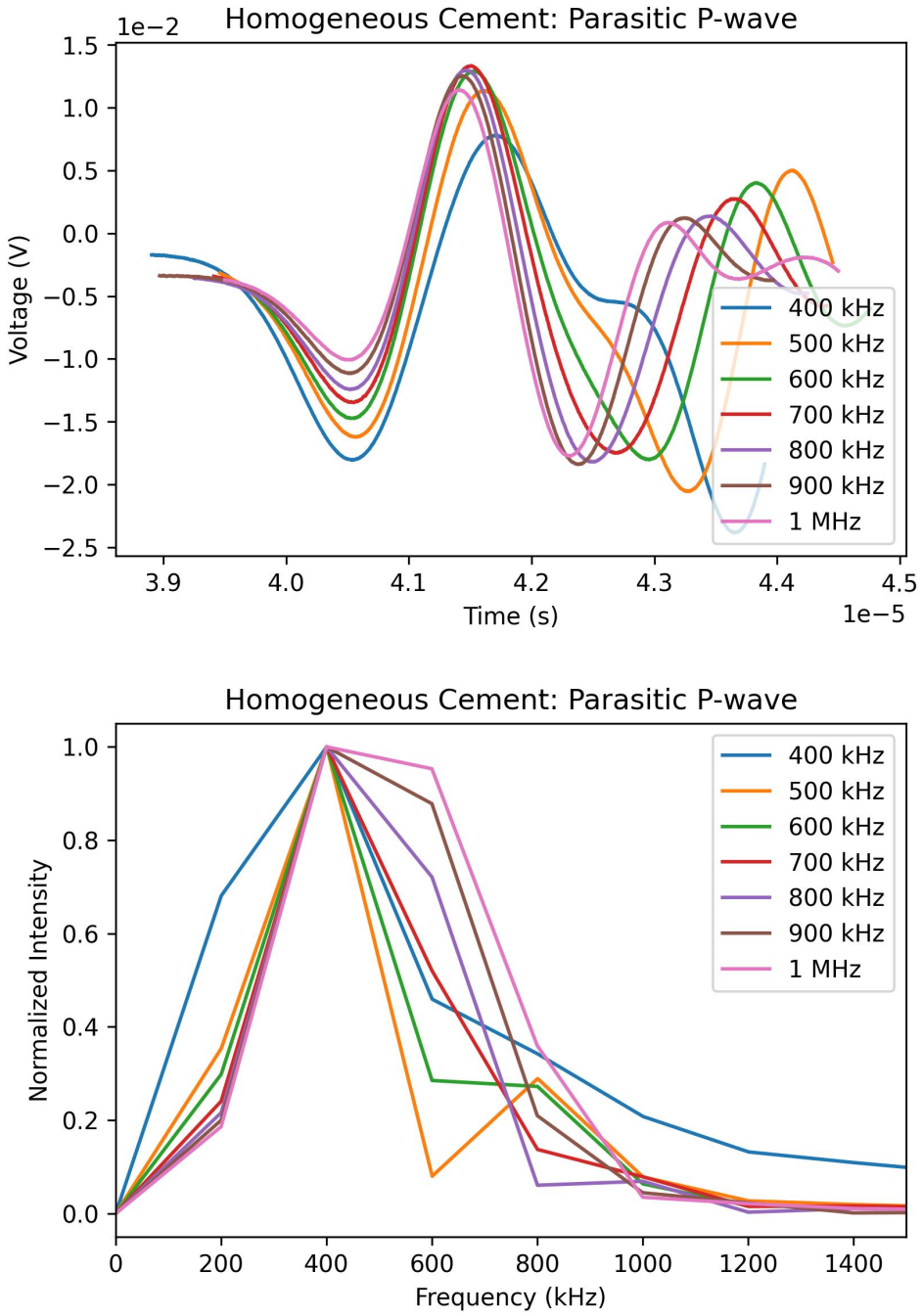

Figure 3.5: Single-cycle pulses from S-wave transducers coupled together with homogeneous cement. This figure illustrates (A) the time domain signals of the parasitic P-wave and (B) the FFT spectra of these signals. FFT spectra were calculated from entire raw waveforms. All spectra have the same central frequency of 400 kHz (see Appendix A for individual uncertainties) and are not in accordance with input frequency.

P-wave components of a single-cycle pulse transmitted through homogeneous cement using S-transducers are independent of the input parameters.

These signatures become increasingly evident visually when we consider 4-cycle pulses. We observe that, for both S-waves and parasitic P-waves, the first cycles of all pulses possess approximately the same period. From Figures 3.7A and 3.8A, we conclude that the coupling signature imposed by S-transducers exists primarily in the first cycle of a discrete signal. Given our learnings from Figure 3.4B, we attribute this likeness in period to the coupling between our transducers and the sample. Specifically, we hypothesize that the act of attempting to initiate a shear wave in a material normal to the transducer face is responsible for the signature. It is well-established that S-transducers produce parasitic P-waves. Hence, we propose that this coupling signature is another phenomenon induced by the edge effects of the transducer. Curiously, after transmission of the first cycle, the signals correct themselves and branch off to their respective frequencies (see Figures 3.7A and 3.8A). This observation tells us that the coupling signature contaminates the frequency component of only the first cycle. The first cycle of a single-cycle pulse encompasses the entire signal. Consequently, the frequency component of a single-cycle pulse is entirely contaminated by the coupling signature, rendering us unable to control the frequency.

P-Transducers Following the same step-wise approach we took with our S-transducers, we build upon the results obtained previously to approach the implementation of a Transient Wave Dynamic Acousto-elastic Testing (TW-DAET) setup using P-transducers. We do so by introducing sample materials between our P-transducer pair to investigate whether they exhibit a coupling signature, as we observed with our S-transducers. Using our sample of homogeneous cement, we transmit a series of single-cycle pulses ranging from 100 kHz to 1 MHz. These time-domain signals are shown in Figure 3.9A.

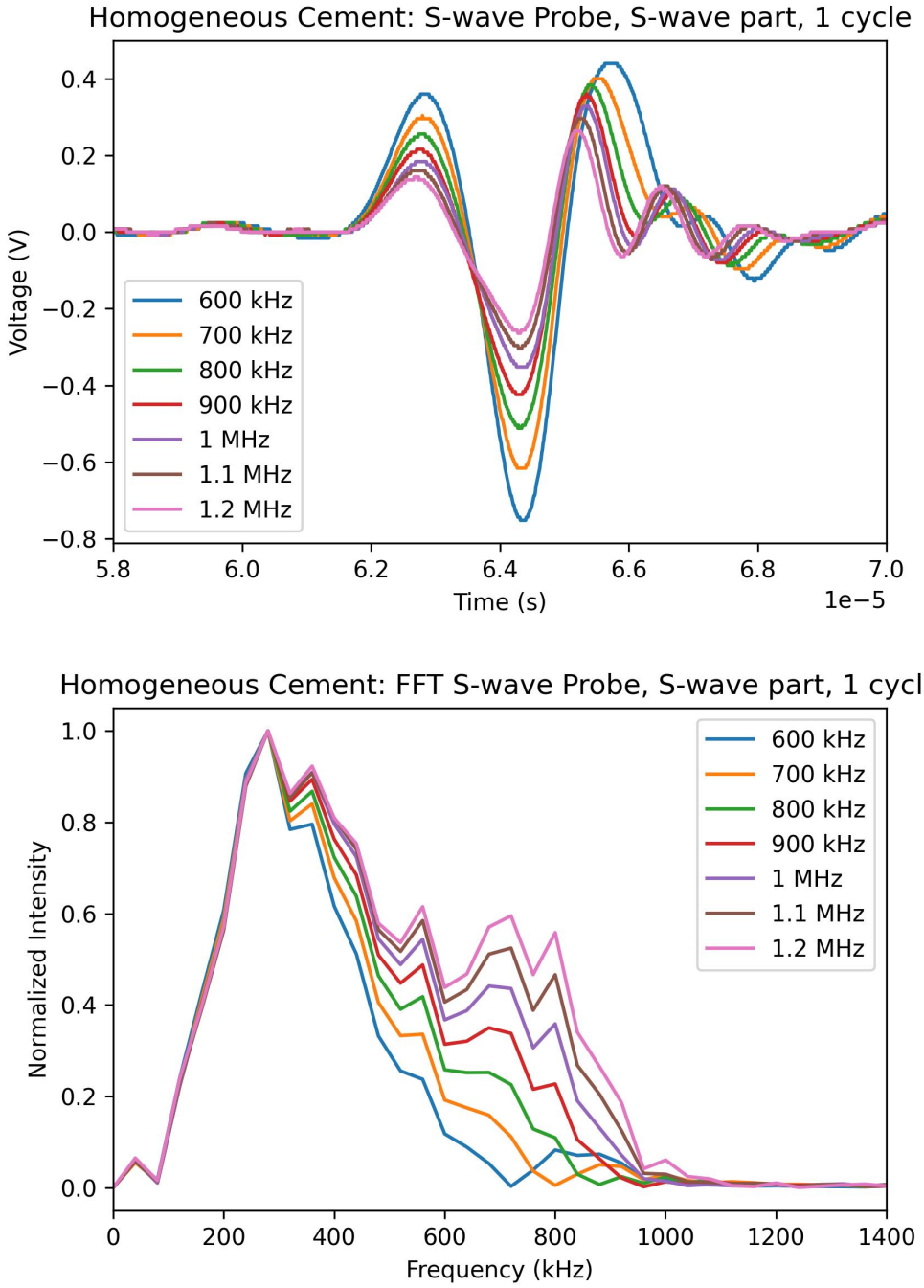

Figure 3.6: Single-cycle pulses from S-wave transducers coupled together with homogeneous cement. Figure (A) illustrates the time domain signals of the resulting S-wave and how the period of the S-wave part of a single-cycle pulse does not change with input frequency. Figure (B) illustrates the FFT spectra of these signals and how the central frequency of the S-wave part of a single-cycle pulse does not change with input frequency. FFT spectra were calculated from entire raw waveforms. All spectra have the same central frequency of 280 kHz (see Appendix A for individual uncertainties) and are not in accordance with input frequency.

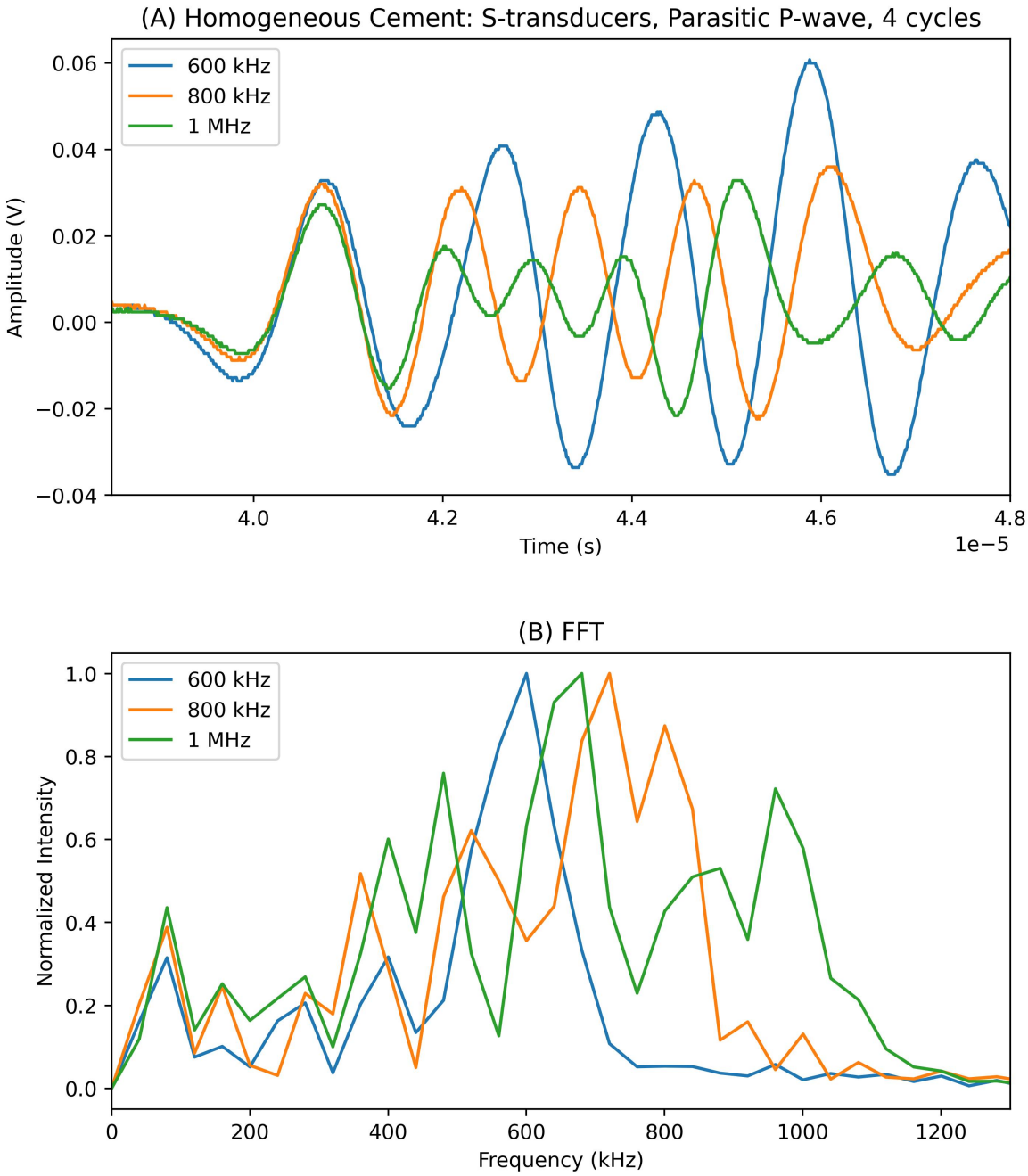

Figure 3.7: Four-cycle pulses from S-wave transducers coupled together with homogeneous cement. This figure illustrates (A) the time domain signals of the parasitic P-wave and (B) the FFT spectra of these signals. FFT spectra were calculated from entire raw waveforms. The period of the first cycle of the parasitic P-wave is independent of the input parameters.

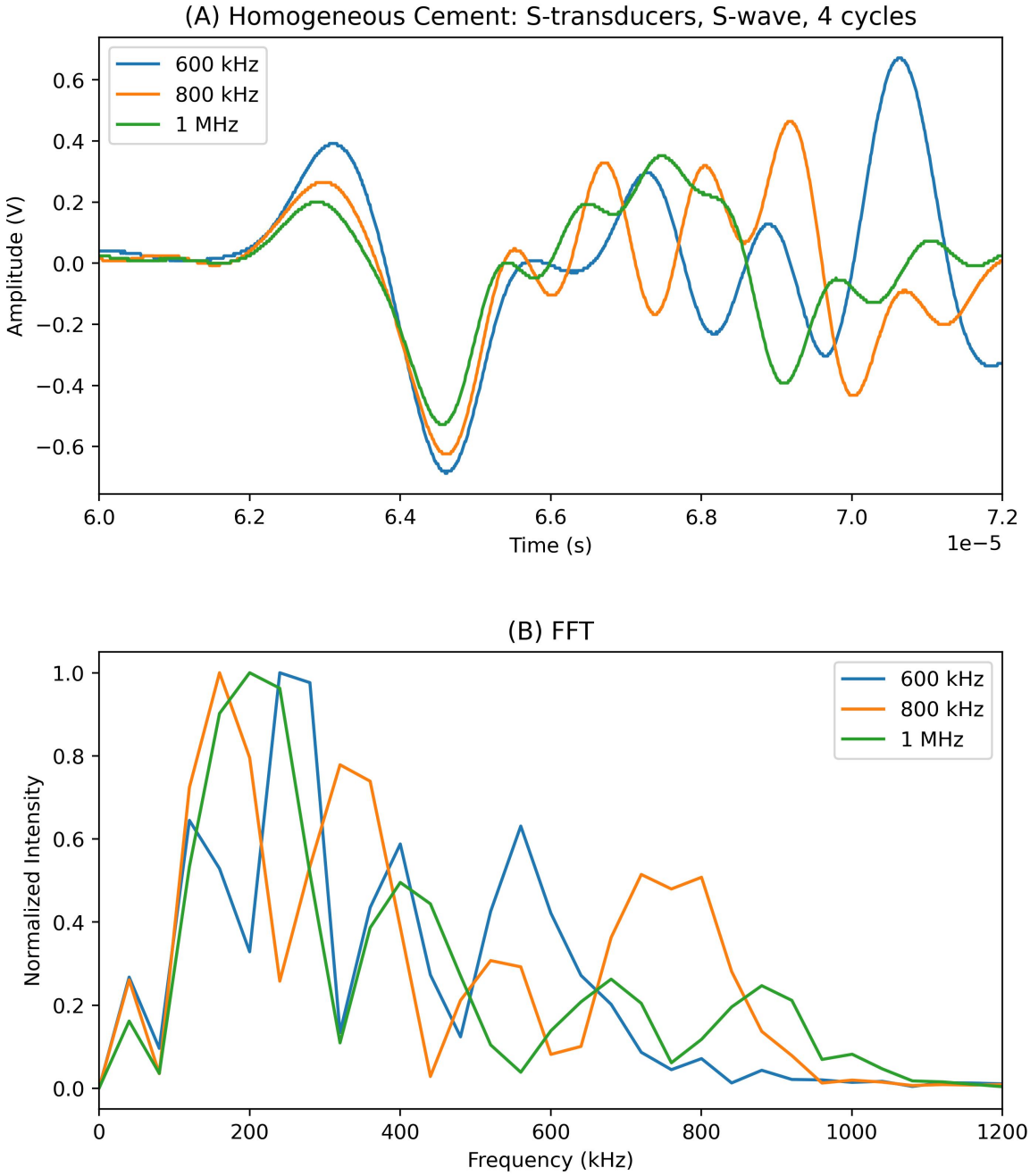

Figure 3.8: Four-cycle pulses from S-wave transducers coupled together with homogeneous cement. This figure illustrates (A) the time domain signals of the S-wave and (B) the FFT spectra of these signals. FFT spectra were calculated from entire raw waveforms. The period of the first cycle of the S-wave is independent of the input parameters

A

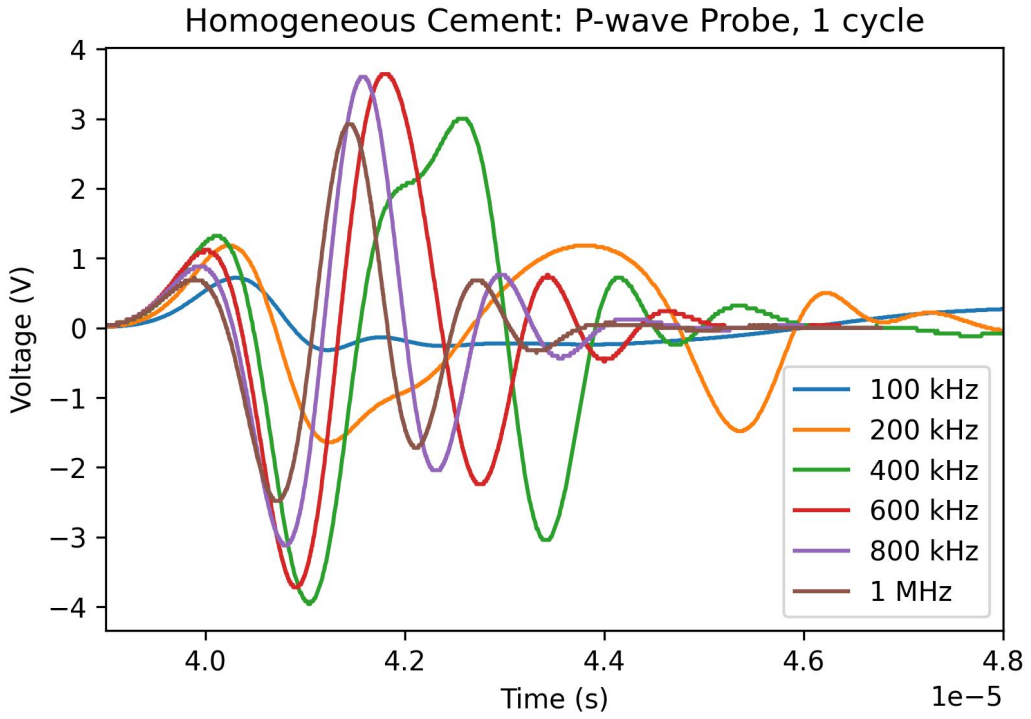

B

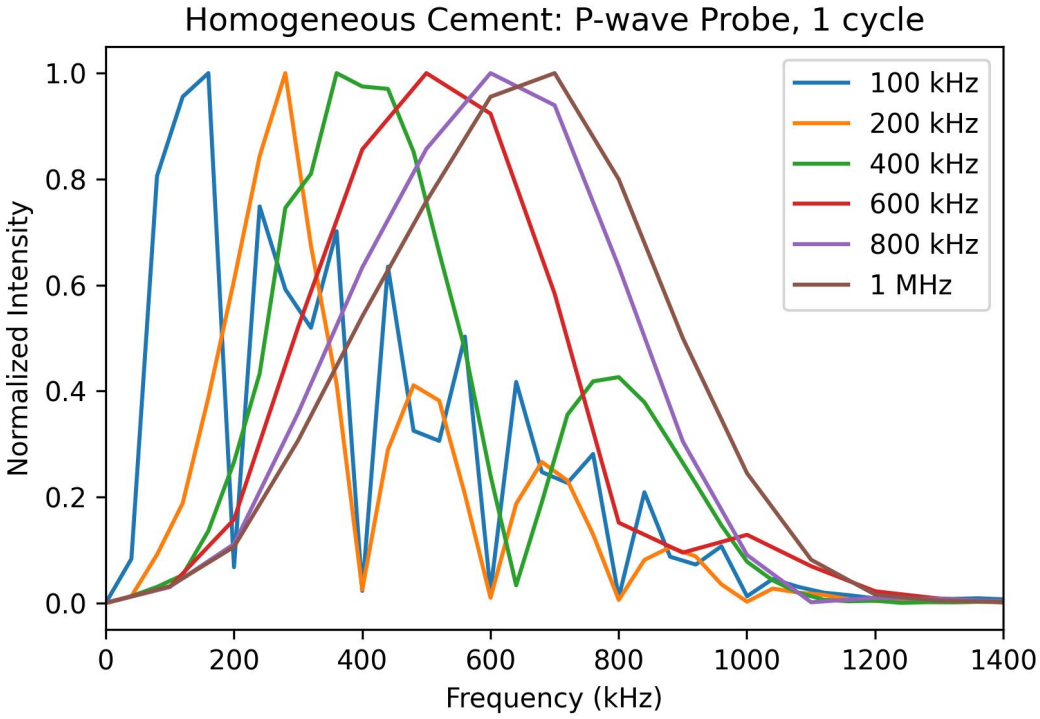

Figure 3.9: Single-cycle pulses from P-transducers coupled together with homogeneous cement. This figure illustrates (A) the time domain signals and (B) the FFT spectra of these signals. FFT spectra were calculated from entire raw waveforms. All spectra have different central frequencies (160±50 kHz, 280±90 kHz, 360±100 kHz, 500±200 kHz, 600±200 kHz, 700±300 kHz).

To evaluate this data in frequency space, in Figure 3.9B, we present the FFT spectra of the raw data from Figure 3.9A. Here, it is apparent that each pulse possesses a different central frequency. This result can be drawn from the fact that the maximum amplitude of each frequency spectrum occurs at different frequencies. Unlike our S-transducer results, these central frequencies are in agreement with their input frequencies, within the range of uncertainty. This result suggests that, unlike our S-transducers, our P-transducers can be used to transmit single-cycle pulses of desired frequencies, even when coupled to a sample material. In the case of the P-transducers, we do not observe a coupling signature, suggesting that it is possible to generate single-cycle pulses with different frequencies. For this reason, we suggest that P-wave transducers are a viable probe transducer option for studying the relationship between probe frequency and elastic non-linearity. Given that our P-transducers are responding as expected, we omit their use in the following section and turn our attention to S-transducers coupled with nonlinear samples.

3.3.3 Nonlinear Samples

Inhomogeneous Cement

We perform one final expansion upon the results obtained previously to approach the implementation of a Transient Wave Dynamic Acousto-elastic Testing (TW-DAET) setup. We do so by introducing nonlinear sample materials between our S-transducers. Firstly, we incorporate a cement sample with an embedded network of evenly spaced (5 mm) copper wires. This is the same sample used to obtain our motivation data (see section 1.4). We transmit a series of single-cycle pulses ranging from 500 kHz to 1 MHz, and we monitor the S-wave component of the output signal. These time-domain signals are shown in Figure 3.10A and the FFT of these pulses are

shown in Figure 3.10B. These FFT spectra were calculated using the time range of $4.85\text{x}10^{-5}$ s to $6\text{x}10^{-5}$ s. In Figure 3.10A, the pulses appear sinusoidal until approximately $6\text{x}10^{-5}$ s. Therefore, this segment of the pulse was selected such that the FFT reflects the region prior to the irregularities. Carefully selecting the same time window for all pulses shown in Figure 3.10 allows us to control the frequency resolution such that all spectra have the same sampling in frequency space (df=90 kHz). Notably, upon introducing a nonlinear material, we observe an increase in the complexity of our time domain signals. Specifically, we note that the supposed "single-cycle" pulses possess several cycles, and their sinusoidal shape is skewed. In Figure 3.10B., we once again observe that the frequency of the elastic waves did not change as the frequency parameter was changed on the generator. Firstly, the central frequencies of our pulses do not agree with the input parameters shown in the legend. Further, all signals ranging from 500 kHz to 1 MHz possess the same central frequency of 350±200 kHz. This result allows us to conclude that the frequency the S-wave component of a single-cycle pulse transmitted through homogeneous cement using S-transducers is independent of the input parameters.

We transmit a series of single-cycle pulses ranging from 600 kHz to 1 MHz through our inhomogeneous cement sample, and we monitor the parasitic P-wave component of the signal. These time-domain signals are shown in Figure 3.11A and the FFT of these pulses are shown in Figure 3.11B. Here, we do not observe the same level of increased complexity in the output as we did with the S-wave component. In Figure 3.11B, we once again observe that the frequency of the parasitic P-waves generated by S-transducers did not change as the frequency parameter was changed on the generator. This is supported by the fact that all signals ranging from 500 kHz to 1 MHz possess the same central frequency of 600±200 kHz.

A

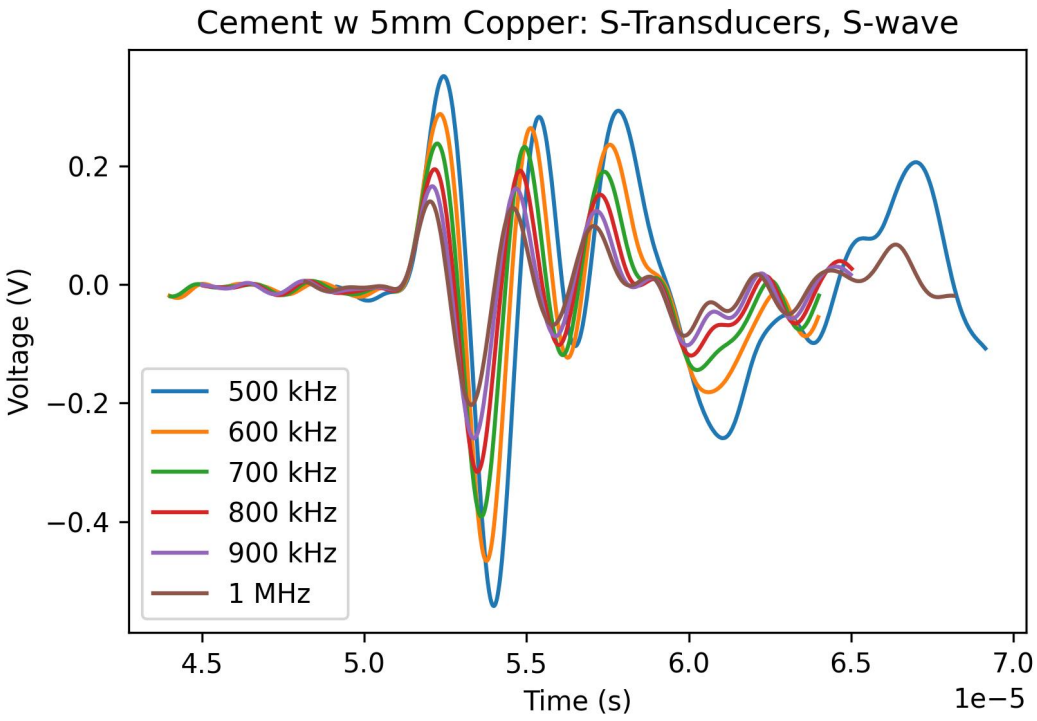

B

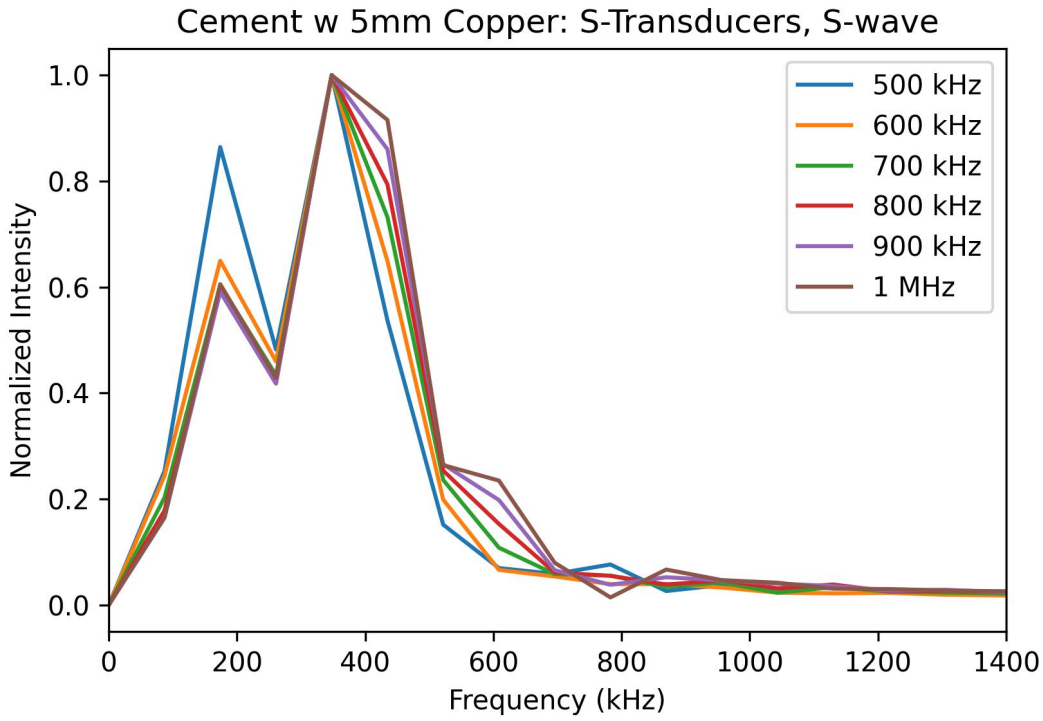

Figure 3.10: Inhomogeneous Cement coupled with S-wave transducers. This figure illustrates the S-wave part of a single-cycle signal. (a) Entire raw waveform in the time-domain. (b) FFT of raw time-domain data between 4.85x10^{-5} s and 6x10^{-5} s. All spectra have the same central frequency of 350±200 kHz and are not in accordance with input frequency.

A

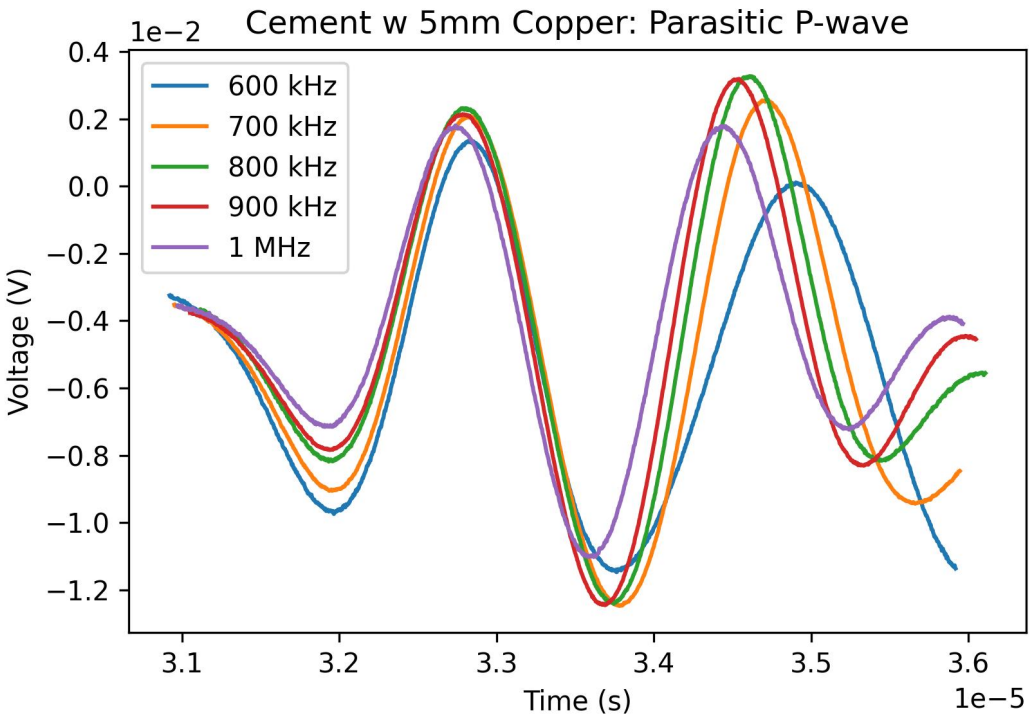

B

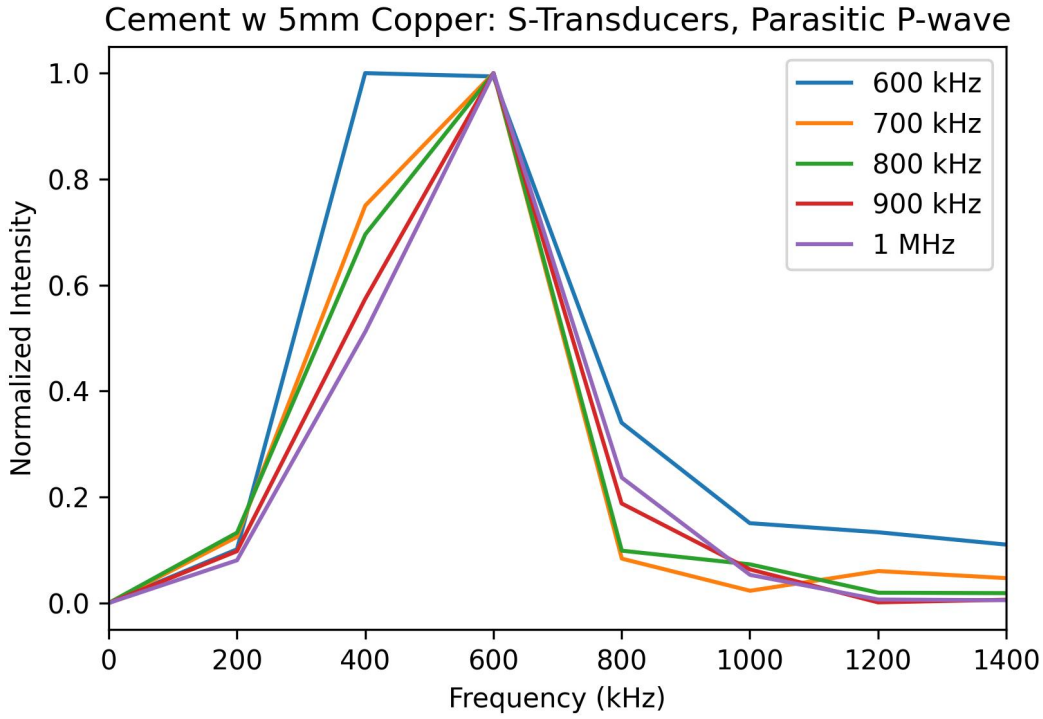

Figure 3.11: Inhomogeneous cement coupled with S-wave transducers. This figure illustrates the parasitic P-wave part of a single-cycle signal. (a) Entire raw time-domain data and (b) the FFT spectra of these raw time-domain data. FFT spectra were calculated from entire raw waveforms. All spectra have the same central frequency of 600±200 kHz and are not all in accordance with input frequency.

We suggest that this central frequency is not repeatable across different setups, nor is it indicative of the bulk material. We have shown that central frequency is highly repeatable within each of the experimental setups, but not between different setups. This is an important distinction, as it potentially highlights the importance of the exact coupling situation between setups. We recall our motivation data, (Figure 1.4), which originated from tracking the parasitic-P-wave component of single-cycle pulses after propagating through the same inhomogeneous cement sample discussed above. This analysis found that all pulses (ranging from 300 kHz to 700 kHz) had the same central frequency of 300±100 kHz. However, our results in Figure 3.11 found that all pulses (ranging from 600 kHz to 1 MHz) had the same central frequency of 600±200 kHz. Given that the identical sample of inhomogeneous cement was examined in both cases, we conclude that the central frequency of the coupling signature is not indicative of the bulk material and has poor repeatability across different setups.

Sandstone

Sandstone is another known nonlinear elastic material [15]. We transmit a series of single-cycle pulses ranging from 600 kHz to 1 MHz through our sandstone sample, and we monitor the S-wave component of the output signal. These time-domain signals are shown in Figure 3.12A and the FFT of these pulses are shown in Figure 3.12B. In Figure 3.12B, we once again observe that the frequency of the elastic waves generated by S-transducers did not change as the frequency parameter was changed on the generator. This is supported by the fact that all pulses ranging from 600 kHz to 1 MHz possess the same central frequency of 300 kHz.

Finally, we transmit a series of single-cycle pulses ranging from 600 kHz to 1 MHz through our sandstone sample, and we monitor the parasitic P-wave component of

A

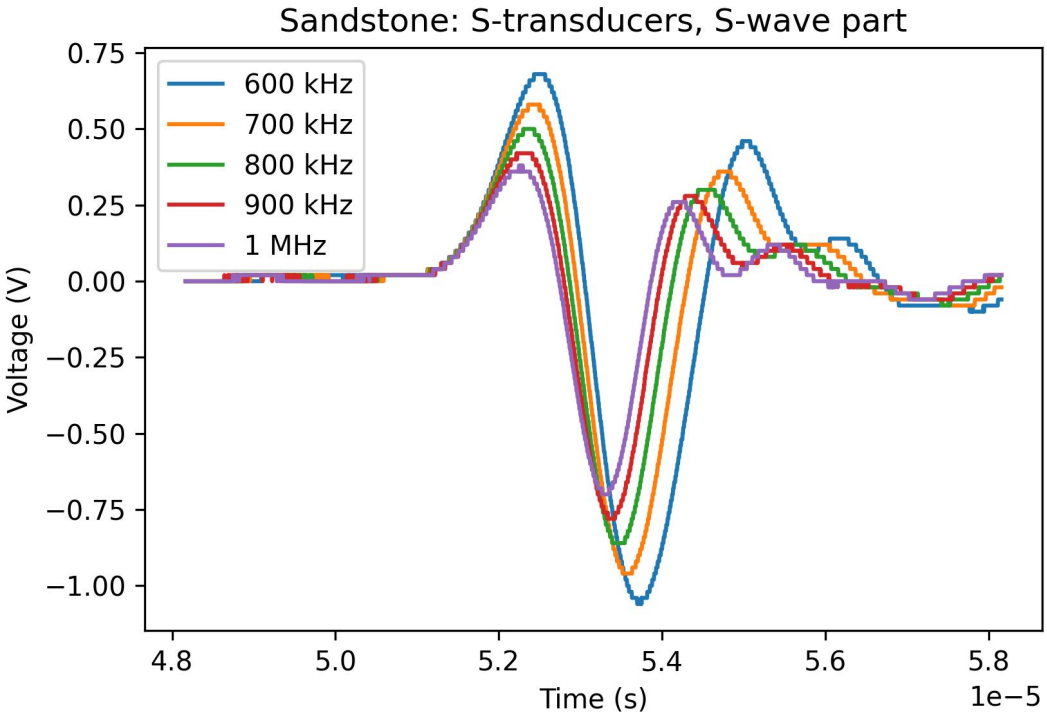

B

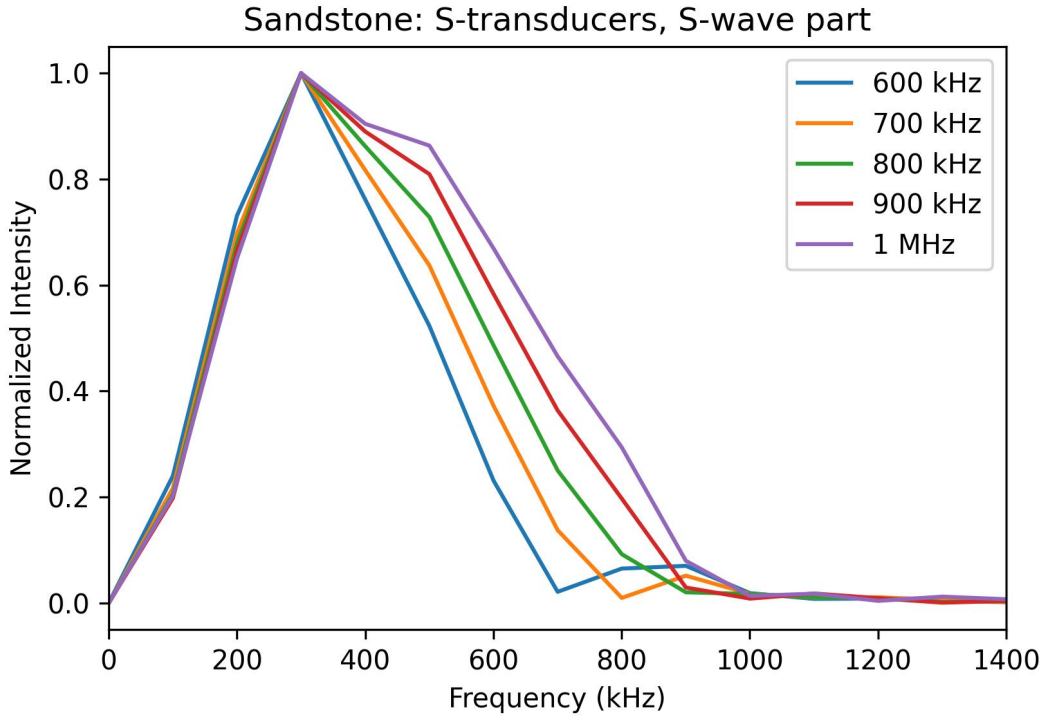

Figure 3.12: Sandstone coupled with S-wave transducers. This figure illustrates the (A) entire time-domain data of the S-wave part of single-cycle pulses and the (b) FFT spectra of the entire time-domain signals. All spectra have the same central frequency of 300 kHz (see Appendix A for individual uncertainties) and are not in accordance with input frequency.

the output signal. These time-domain signals are shown in Figure 3.13A and the FFT of these pulses are shown in Figure 3.13B. In Figure 3.13B, we once again observe that the frequency of the elastic waves generated by S-transducers did not change as the frequency parameter was changed on the generator. This is supported by the fact that all pulses ranging from 600 kHz to 1 MHz possess the same central frequency of 160±70 kHz. With sandstone, we observe the complexity of our signal increase for the parasitic P-wave component of the signal but not for the S-wave component. This observation is the opposite of that for inhomogeneous cement, where the S-wave component of the signal was more complicated, but the parasitic P-wave was not.

When coupled to our sample materials, both elastically linear and nonlinear, our shear wave transducers generate a coupling signature pulse, whose frequency is independent of the waveform frequency set on the generator. When a pulse consists of multiple cycles, the first cycle of the pulse is contaminated by the coupling signature. Furthermore, this coupling signature is observed in both the parasitic P-wave and the S-wave component of these pulses. Interestingly, both components have different coupling signatures (different central frequencies). When a single-cycle pulse is sent from a shear wave transducer, the entire pulse is contaminated by the coupling signature. Therefore, the frequency of a single-cycle pulse will reflect the coupling signature rather than the frequency set on the generator. In other words, for a given coupled system, we cannot reliably change the frequency of a single-cycle pulse from a shear wave transducer. For this reason, shear wave transducers should not be used to study the relationship between probe frequency and elastic non-linearity. We found that this "coupling signature" is present for both the parasitic P-wave component of the signal, as well as the intentional S-wave component. However, it should be noted that the parasitic P-wave and the S-wave pulses have different coupling signatures with different central frequencies. The signature becomes more visually evident when we

A

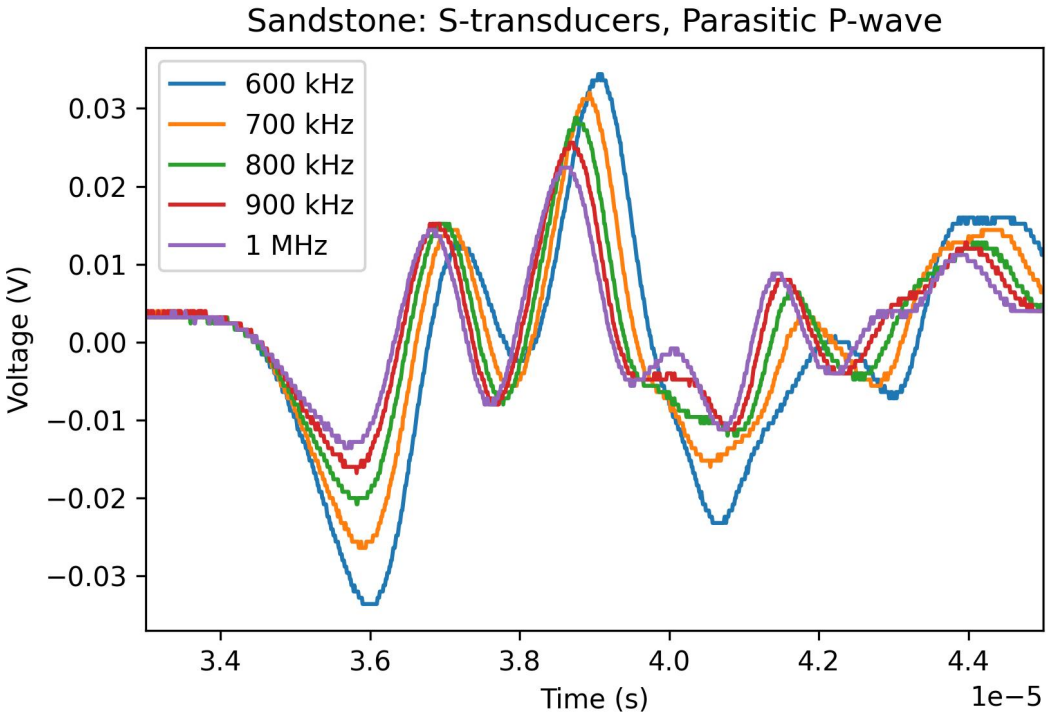

B

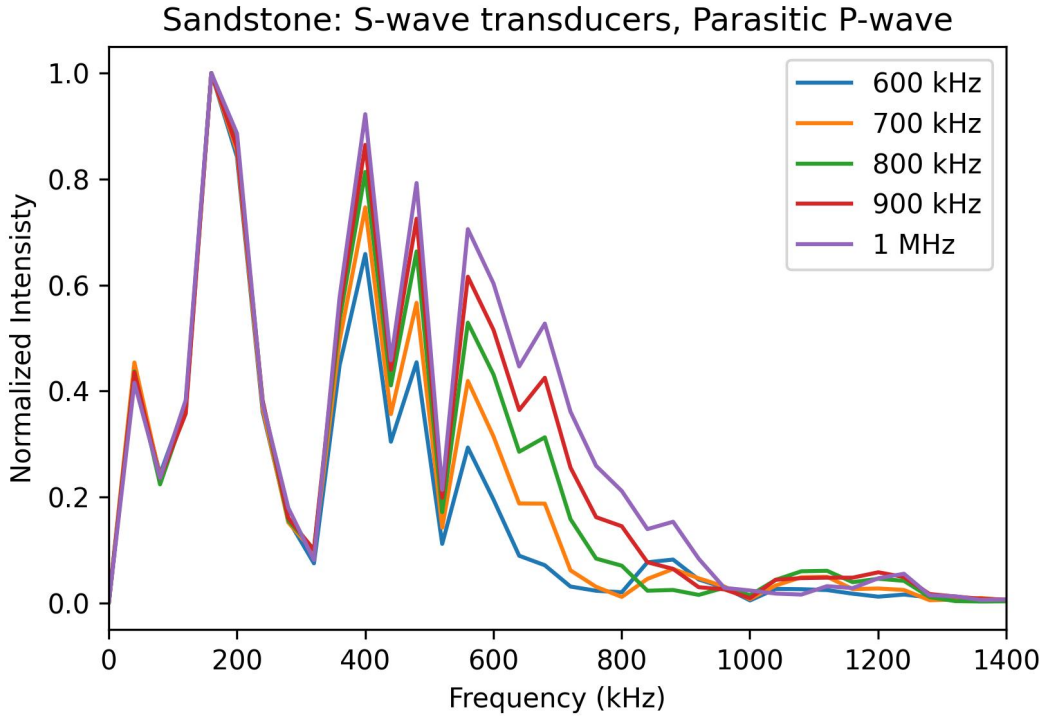

Figure 3.13: Sandstone coupled with S-wave transducers. This figure illustrates the entire time-domain data of the parasitic P-wave of a single-cycle pulse and (b) the FFT spectra of the entire signals. All signals possess the same central frequency of 160±200 kHz, and are not in agreement with input frequency.

observe more cycles. However, the signature does not appear for continuous signals, suggesting that it is a result of the transducers initiating a pulse.

Chapter 4

Conclusions

4.1 Summary

In all but one case, sending a series of ultrasonic pulses through various setups found the central frequency of pulses changed as we changed the input frequency. The exceptional case occurred when we coupled S-transducers to a sample material and sent a series of single-cycle pulses. Only in this case did we observe that for a given setup all pulses possessed the same central frequency, regardless of the input frequency. When a pulse consists of multiple cycles, a signal artifact exists in the first cycle of the pulse. When a continuous pulse is transmitted, no coupling signature is observed. This further suggests that the coupling signature is attributed to the initiation of a pulse sequence because a continuous signal has no discrete start or stop region. When a single-cycle pulse is sent from a shear wave transducer, the entire pulse is contaminated by the coupling signature. Moreover, we found that a coupling signature is present for both the parasitic P-wave component of the signal, as well as the S-wave component. However, the parasitic P-wave and the S-wave pulses have different coupling signatures

with different central frequencies. Therefore, the frequency of a single-cycle pulse will reflect the coupling signature rather than the waveform frequency set on the generator. In other words, for a given coupled system, we cannot reliably change the frequency of a single-cycle pulse from a shear wave transducer. For this reason, shear wave transducers should not be used to study the relationship between probe frequency and elastic non-linearity. These observations are consistent among linear and nonlinear materials. Hence, we speculate that this frequency discrepancy is attributed to wave interactions at the interface between the transducer's active face and the sample material, and not induced by inhomogeneities in the sample. When a shear force is perpendicular to a flat surface, we speculate that the initiation of a pulse causes a slipping between surfaces at the interface. Further, the transducer's active surface and the sample material are not infinitely long, so edge effects are expected. It is possible that the bevelled outer edge of the transducer's active face generates S-wave energy which diffracts. Without the presence of a sample material between the transducers, these diffracted waves have no mode of arriving at the receiver, and thus, we do not observe the slipping and/or diffraction effects. Lastly, in the case of the P-transducers, our results suggest that it is possible to generate single-cycle pulses with different frequencies. Hence, we conclude that P-transducers do not produce a coupling signature which contaminates the first cycle. For this reason, P-transducers are a viable option in probe transducer selection when studying the relationship between probe frequency and elastic non-linearity.

Overall, we conclude that best practices for future work should monitor waveforms passing through the sample, and not just input waveforms. This conclusion stems from our newfound understanding of how transducer responses are related to coupling and how the properties of ultrasonic pulses change as they propagate through our experimental setup. The results from the experiments in this thesis have allowed us to

establish a baseline for what we should expect to see in terms of output pulses and conclude that the frequency conversion reported in Chapter 1 is not a result of dysfunctional equipment. Rather, it should be attributed to how our S-transducers behave in coupled conditions. When coupled, S-transducers generate a coupling signature whose frequency is independent of the frequency we set on the waveform generator. Therefore, we conclude that S-wave transducers are not a viable option when selecting a probe transducer to generate single-cycle pulses for measuring the relationship between probe frequency and nonlinear elasticity.

4.2 Future Work

Can we generalize our theory? It is possible that our S-transducers have been exposed to conditions which may have altered the way they behave in coupled conditions. To address this possibility, we propose repeating a series of experiments from Chapter 3 with several new S-transducers. This will allow us to make broader claims regarding the behaviour of S-transducers at large, rather than just the small sample size of transducers in our acoustics laboratory.

Multi-cycle probes? Returning to the initial research which motivated this thesis, we propose running a series of experiments using the Transient Wave Dynamic Acousto-elastic Testing (TW-DAET) setup to address the frequency dependence of nonlinear wave interactions. As we've shown throughout this thesis, obtaining reliable measurements of single-cycle pulse frequency is challenging, and increasing the number of cycles greatly improves our peak resolution. Using a well-characterized material, and a multi-cycle probe wave, we intend to compare our nonlinear responses

from our single-cycle probe to that of our multi-cycle probe to determine if increasing probe duration affects our non-linear results. In TW-DAET, we monitor changes in the probe induced by the pump, which is referred to as the perturbed probe. In theory, a multi-cycle probe is a viable option. However, we question whether or not increasing the duration of the probe will reduce its ability to resolve finer interactions. Further, the use of multi-cycle probes may complicate our interpretation because we assume that the pump signal is unchanged during the passage of the probe, which may not be true when the probe length is increased. If the results are consistent among both single and multi-cycle probes, we can proceed with nonlinear scans using multi-cycle probes, which would greatly improve our ability to measure the frequency of these pulses. This would allow us to proceed with our investigation into the frequency dependence of nonlinear wave interaction with our current TW-DAET setup, all the while having confidence in the frequency content of our ultrasonic pulses.

Can a coupling signature be used to identify samples? Our preliminary results suggest that the central frequency of coupling signatures is not repeatable, nor are they indicative of the bulk material. We drew this conclusion after comparing the central frequency spectra from our motivation data in Chapter 1 (Figure 1.4; repeated in Figure 4.1A) and our results when repeated using the same sample, transducers and pulses (Figure 3.11; repeated in Figure 4.1B). In both cases, we tracked the parasitic-P-wave component of single-cycle pulses after propagating through the same exact inhomogeneous cement sample. However, these experiments were conducted several months apart, over slightly different frequency ranges and several factors such as temperature, humidity, the volume of couplant, and the force on the bar clamp were not controlled. In comparing the two, all pulses in the motivation data (ranging from 300 kHz to 700 kHz) had the same central frequency of 300±100 kHz. However, our

results in Figure 3.11 found that all pulses (ranging from 600 kHz to 1 MHz) had the same central frequency of 600±200 kHz. These two central frequencies are in agreement within their ranges of uncertainty, but this is an unconvincing agreement due to the large uncertainties associated with these measurements. Given that the identical sample of inhomogeneous cement was examined in both cases, we theorize that the central frequency of the coupling signature is not indicative of the bulk material and has poor repeatability. To investigate this theory, we propose investigating how the coupling signature is affected by changing the dimensions of the sample materials. This will indicate whether the coupling signature can provide insight into the properties of the bulk material or if it is contingent on the geometry of the setup. Further, we propose using a variety of different coupling conditions (e.g. volume of couplant and amount of force on the bar clamp) and, eventually, different sample materials to determine if any properties of the coupling signature are unique to each coupled system, addressing the question of whether this single-cycle pulse could be used to identify unknown samples.

What is behind the parasitic P-wave? Finally, we hypothesize that parasitic P-waves are a result of the edge of our transducer surface exhibiting motion in the normal direction when in contact with a solid. Notably, we did not observe parasitic P-waves when our S-transducers were tested individually using laser vibrometry. We positioned the laser directly in the centre of the transducer's active surface. Therefore, it is unsurprising that parasitic P-waves were not observed. We propose a future experiment using the laser vibrometry technique, which involves positioning reflective tape on the outer edges of the transducer's active surface and positioning the laser on said edge. This would provide insight as to if parasitic P-waves are inherently produced by the transducer edges, or if they are a result of the edges interacting

A

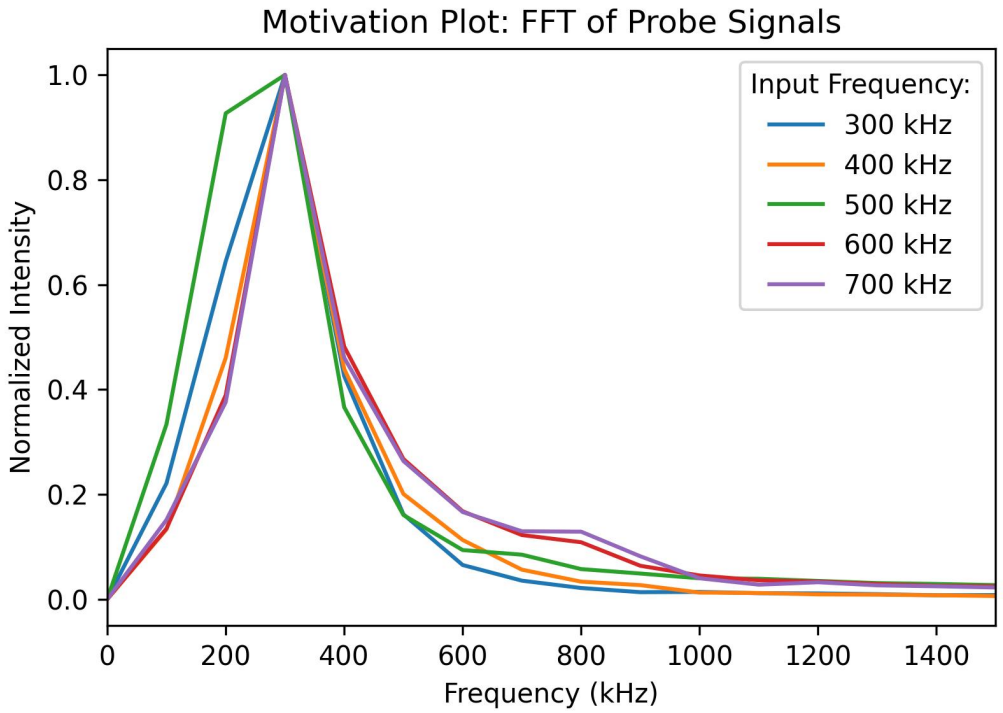

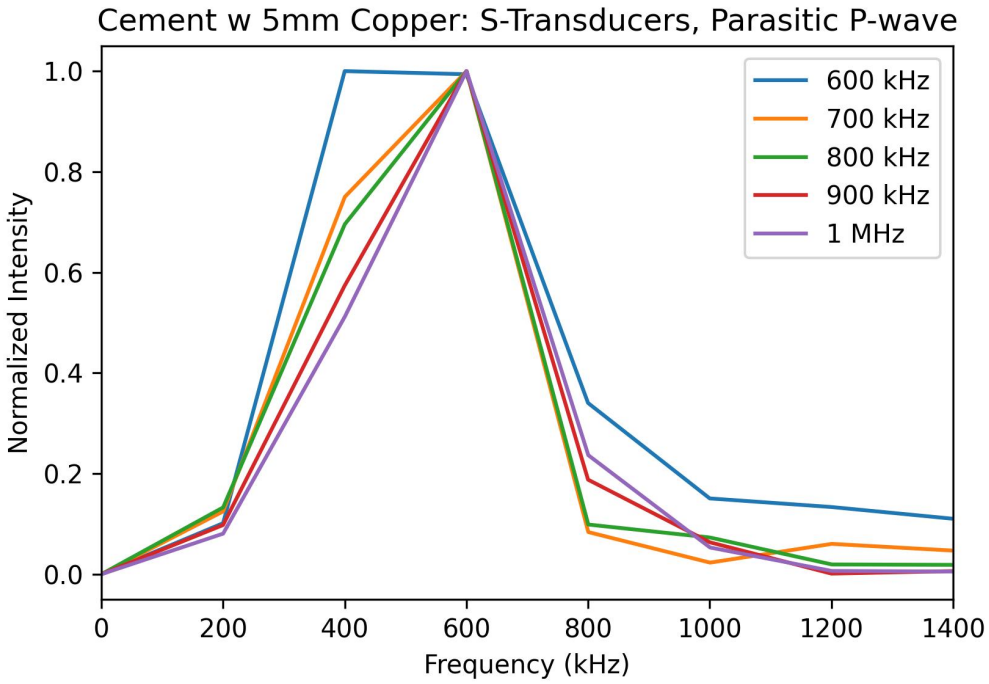

B

Figure 4.1: FFT spectra of the parasitic P-wave component of single-cycle ultrasonic pulses after propagating through inhomogeneous cement (cement with an embedded network of evenly spaced (5mm) copper wires) coupled with S-wave transducers. (a) Figure 1.4 repeated. All signals possess the same central frequency of 300±100 kHz. (b) Figure 3.11 repeated. All signals possess the same central frequency of 600±200 kHz.

with a solid. To address the latter, given we also do not observe a parasitic P-wave when we couple two S-transducers together without a sample, we propose examining if parasitic P-waves occur when pulses travel through a long sample whose interface is smaller than the active surface of the transducer. In other words, the face of the solid is contained within the transducer's surface and therefore does not interact with the edges of the transducer. If we do not observe parasitic P-waves, we can conclude that the edge effect is responsible. Another possibility is that the lack of parasitic P-wave production is a result of travel time restrictions. We propose examining if parasitic P-waves occur when pulses travel through a thin intermediate sample. This would address whether the lack of P-wave production is a matter of limited travel time (The S-wave is recorded almost immediately, leaving no time to distinguish between P-wave and S-wave arrivals). Interestingly, just as in the case of the coupling signature, we observe the parasitic P-wave only when transducers are loaded with a sample. Furthermore, we do not observe either phenomenon in P-transducers, suggesting that perhaps there exists a link between these two phenomena.

Bibliography

[1] Francis Birch. The velocity of compressional waves in rocks to 10 kilobars: 1. *Journal of Geophysical Research*, 65(4):1083–1102, 1960.

[2] Christopher Brown, Timothy Norman, Vincent Kish, Thomas Gruen, and John Blaha. Time-dependent circumferential deformation of cortical bone upon internal radial loading. *Journal of biomechanical engineering*, 124:456–61, 09 2002.

[3] John M Cimbala. Statistical analysis: Fourier transforms, dfts, and ffts. 2010.

[4] JA Gallego-Juarez. Piezoelectric ceramics and ultrasonic transducers. *Journal of Physics E: Scientific Instruments*, 22(10):804, 1989.

[5] Thomas Gallot, Alison Malcolm, Thomas L Szabo, Stephen Brown, Daniel Burns, and Michael Fehler. Characterizing the nonlinear interaction of s-and p-waves in a rock sample. *Journal of applied physics*, 117(3):034902, 2015.

[6] PA Gaydecki, FM Burdekin, W Damaj, and DG John. The propagation and attenuation of medium-frequency ultrasonic waves in concrete: a signal analytical approach. *Measurement Science and Technology*, 3(1):126, 1992.

[7] Karl F Graff. *Wave motion in elastic solids*. Courier Corporation, 2012.

[8] Scott P Grogan and Cristin A Mount. *Ultrasound Physics and Instrumentation*. StatPearls Publishing, April 2022.

[9] Tomáš Harčarik, Jozef Bocko, and Kristína Maslákováá. Frequency analysis of acoustic signal using the fast fourier transformation in matlab. *Procedia Engineering*, 48:199–204, 2012.

[10] Henry E Heffner and Rickye S Heffner. Hearing ranges of laboratory animals. *Journal of the American Association for Laboratory Animal Science*, 46(1):20–22, 2007.

[11] Randall Dewey Knight. *Physics for scientists and engineers: a strategic approach with modern physics*. Pearson New York, NY, 2017.

[12] Pascal Laugier and Guillaume Haïat. Introduction to the physics of ultrasound. *Bone quantitative ultrasound*, pages 29–45, 2011.

[13] Etgar C Levy and Moshe Horowitz. Single-cycle radio-frequency pulse generation by an optoelectronic oscillator. *Optics Express*, 19(18):17599–17608, 2011.

[14] Meina Li and Youn Tae Kim. Feasibility analysis on the use of ultrasonic communications for body sensor networks. *Sensors*, 18(12):4496, 2018.

[15] G Douglas Meegan Jr, Paul A Johnson, Robert A Guyer, and Katherine R McCall. Observations of nonlinear elastic wave behavior in sandstone. *The Journal of the Acoustical Society of America*, 94(6):3387–3391, 1993.

[16] M Muller, D Mitton, M Talmant, P Johnson, and P Laugier. Nonlinear ultrasound can detect accumulated damage in human bone. *Journal of Biomechanics*, 41(5):1062–1068, 2008.

[17] Jacob Edward Newman. Dependence of elastic nonlinearity on aligned inhomogeneities. Master's thesis, Memorial University of Newfoundland, 2021.

[18] Travis E Oliphant et al. *A guide to NumPy*, volume 1. Trelgol Publishing USA, 2006.

[19] Olympus. Ultrasonic transducers technical notes, 2019.

[20] G Renaud, Julie Rivière, C Larmat, JT Rutledge, RC Lee, RA Guyer, K Stokoe, and PA Johnson. In situ characterization of shallow elastic nonlinear parameters with dynamic acoustoelastic testing. *Journal of Geophysical Research: Solid Earth*, 119(9):6907–6923, 2014.

[21] Guillaume Renaud, Samuel Calle, Jean-Pierre Remenieras, and Marielle Defontaine. Exploration of trabecular bone nonlinear elasticity using time-of-flight modulation. *IEEE Transactions on Ultrasonics, Ferroelectrics, and Frequency Control*, 55(7):1497–1507, 2008.

[22] Jacques Rivière, Lucas Pimienta, Marco Scuderi, Thibault Candela, Parisa Shokouhi, Jérôme Fortin, Alexandre Schubnel, Chris Marone, and Paul A Johnson. Frequency, pressure, and strain dependence of nonlinear elasticity in berea sandstone. *Geophysical Research Letters*, 43(7):3226–3236, 2016.

[23] Jacques Riviere and Philippe Roux. Dynamic acousto-elastic testing with an ultrasonic tomography probe: Application to fractured rock characterization. *The Journal of the Acoustical Society of America*, 142(4):2723–2723, 2017.

[24] Montaña Rufo, Antonio Jiménez, Jesús M Paniagua, and Alberto González-Mohíno. Ultrasound assessment of honey using fast fourier transform. *Sensors*, 21(20):6748, 2021.

[25] Oleg A Sapozhnikov, Andrey V Morozov, and Dominique Cathignol. Piezoelectric transducer surface vibration characterization using acoustic holography and laser vibrometry. In *IEEE Ultrasonics Symposium, 2004*, volume 1, pages 161–164. IEEE, 2004.

[26] Jonathan Simpson, Kasper van Wijk, Ludmila Adam, and Caitlin Smith. Laser ultrasonic measurements to estimate the elastic properties of rock samples under in situ conditions. *Review of Scientific Instruments*, 90(11):114503, 2019.

[27] Wenyu Tang, Hang Lin, Yifan Chen, Jingjing Feng, and Huihua Hu. Mechanical characteristics and acoustic emission characteristics of mortar-rock binary medium. *Buildings*, 12(5):665, 2022.

[28] Mihailo Dimitrije Trifunac and Vincent W Lee. Frequency dependent attenuation of strong earthquake ground motion. *Soil Dynamics and Earthquake Engineering*, 9(1):3–15, 1990.

[29] Pauli Virtanen, Ralf Gommers, Travis E Oliphant, Matt Haberland, Tyler Reddy, David Cournapeau, Evgeni Burovski, Pearu Peterson, Warren Weckesser, Jonathan Bright, et al. Scipy 1.0: fundamental algorithms for scientific computing in python. *Nature methods*, 17(3):261–272, 2020.

[30] Quang Anh Vu, Vincent Garnier, Jean François Chaix, Cédric Payan, Martin Lott, and Jesus N Eiras. Concrete cover characterisation using dynamic acoustoelastic testing and rayleigh waves. *Construction and Building Materials*, 114:87–97, 2016.

[31] Dingguo Xiao, Qiong Fan, Chunguang Xu, and Xiuhua Zhang. Measurement methods of ultrasonic transducer sensitivity. *Ultrasonics*, 68:150–154, 2016.

[32] Alexey Yurikov, Nazanin Nourifard, Marina Pervukhina, and Maxim Lebedev. Laboratory ultrasonic measurements: Shear transducers for compressional waves. *The Leading Edge*, 38(5):392–399, 2019.

[33] Shuzeng Zhang, Canhui Cheng, Xiongbing Li, and Tribikram Kundu. Fast fourier transform method for determining velocities of ultrasonic rayleigh waves using a comb transducer. *Ultrasonics*, 124:106754, 2022.

Appendix A

Central Frequencies

Experiment	**Input Frequency** (kHz)	**Central Frequency** (kHz)	± (kHz)	**df** (kHz)
Wave generator	100	80	50	20
to oscilloscope	300	300	200	100
– 1 cycle	500	400	300	200
(Figure 2.7)	800	600	500	200
	1000	800	500	200
Wave generator	100	100	20	20
to oscilloscope	200	200	30	20
– 4 cycles	400	400	50	50
(Figure 2.9)	600	600	100	50
	800	800	100	100
	1000	1000	200	100
Wave generator	100	100	4	20
to oscilloscope	200	200	4	20

– continuous	400	400	10	50
(Figure 2.10)	600	600	10	50
	800	800	20	100
	1000	1000	20	100
Single S-transducer	50	40	20	10
– 1 cycle (full)	100	100	40	10
(Figure 2.13B)	150	120	50	10
	200	120	60	10
Single S-transducer	50	60	50	40
– 1 cycle (cropped)	100	120	40	40
(Figure 2.13C)	150	120	50	40
	200	120	60	40
Single S1-transducer	50	50	2	2
– 10 cycles	100	100	4	5
(Figure 2.15)	200	200	10	5
Single S2-transducer	50	50	3	1
– 10 cycles	100	100	4	2
(Figure 2.15)	200	200	10	10
Single P2-transducer	50	50	3	2
– 10 cycles	100	100	5	2
(Figure 2.15)	200	200	10	2
Single P1-transducer	50	50	3	2
– 10 cycles	100	100	4	5
(Figure 2.15)	200	200	10	10
S-transducer pair	200	200	50	20
No sample – 1 cycle	400	400	200	100

(Figure 3.4)	600	700	300	100
	800	900	300	100
	1000	900	300	100
P-transducer pair	100	100	50	10
No sample - 1 cycle	200	180	100	20
(Figure 3.3)	400	440	200	40
	600	600	300	100
	800	800	400	100
	1000	800	400	100
Homogeneous Cement	100	160	50	40
P-transducers	200	280	90	40
1 cycle	400	360	100	40
(Figure 3.9)	600	500	200	100
	800	600	200	100
	1000	700	300	100
Homogeneous Cement	400	400	300	200
S-transducers	500	400	100	200
Parasitic P-wave	600	400	200	200
1 cycle	700	400	200	200
(Figure 3.5)	800	400	200	200
	900	400	200	200
	1000	400	200	200
Homogeneous Cement	600	280	200	40
S-transducers	700	280	200	40
S-wave – 1 cycle	800	280	200	40
(Figure 3.6)	900	280	200	40

	1000	280	200	40
	1100	280	300	40
	1200	280	300	40
*Inhomogeneous Cement	500	350	200	90
S-transducers	600	350	200	90
S-wave – 1 cycle	700	350	200	90
(Figure 3.10)	800	350	200	90
	900	350	200	90
	1000	350	200	90
Inhomogeneous Cement	600	600	200	200
S-transducers	700	600	200	200
Parasitic P-wave	800	600	200	200
1 cycle	900	600	200	200
(Figure 3.11)	1000	600	200	200
Sandstone	600	160	70	40
S-transducers	700	160	70	40
P-wave	800	160	70	40
1 cycle	900	160	70	40
(Figure 3.13)	1000	160	70	40
Sandstone	600	300	200	100
S-transducers	700	300	200	100
S-wave - 1 cycle	800	300	200	100
(Figure 3.12)	900	300	200	100
	1000	300	300	100

Table A.1: Central frequencies. All FFT spectra were calculated using the entire raw data set, unless stated otherwise (*). The central frequency of all FFT spectra in this thesis are reported as the frequency where the maximum spectral intensity occurs. Each spectrum was fitted with a gaussian and the full width at half maximum (FWHM) was calculated and half this value is reported as the uncertainty ($\pm$) in the central frequency.